Science Advances
AAAS

Manuscript Template

FRONT MATTER

Progression of Ocean Interior Acidification over the Industrial Era

Short Title: Progression of Ocean Interior Acidification

Jens D. Müller[1*], Nicolas Gruber[1]

[1]Environmental Physics, Institute of Biogeochemistry and Pollutant Dynamics, ETH Zurich, Zurich, Switzerland.

*Corresponding author. Email: jensdaniel.mueller@usys.ethz.ch

Abstract

Ocean acidification driven by the uptake of anthropogenic CO_2 represents a major threat to ocean ecosystems, yet little is known about its progression beneath the surface. Here, we reconstruct the history of ocean interior acidification (OIA) from 1800 to 2014 on the basis of observation-based estimates of the accumulation of anthropogenic carbon. Across the top 100 m and over the industrial era, the saturation state of aragonite (Ω_{arag}) and pH = -log[H^+] decreased by more than 0.6 and 0.1, respectively, with a progress of nearly 50% over the last 20 years (1994-2014). While the magnitude of the Ω_{arag} change decreases uniformly with depth, the magnitude of the pH decrease exhibits a distinct maximum in the upper thermocline. Since 1800, the saturation horizon (Ω_{arag}=1) shoaled by more than 200 m, approaching the euphotic zone in several regions, especially in the Southern Ocean, and exposing many organisms to corrosive conditions.

Teaser

The rapid downward progression of anthropogenic carbon accelerates ocean interior acidification and threatens marine biota.

MAIN TEXT

Introduction

The ocean currently absorbs around a quarter of the annual anthropogenic CO_2 emission (*1–3*). While this net uptake of anthropogenic CO_2 mitigates climate change, it also acidifies the world's most voluminous ecosystem (*4–6*). Ocean Acidification (OA) comprises multiple changes in the marine CO_2 system, including the increase of the proton (H^+) concentration leading to a reduction of pH ($-\log[H^+]$), as well as a decline of the carbonate ion (CO_3^{2-}) concentration, which lowers the saturation state (Ω) of carbonate minerals (Wolf-Gladrow and Zeebe, 2001). These changes are expected to have substantial impacts on the fitness of many organisms affecting also ecosystem functioning (*5*, *7–9*).

So far, most OA studies have focused exclusively on the surface ocean, although it is well established that the downward transport of anthropogenic CO_2 (C_{ant}) acidifies the ocean also at depth. Driven by the downward progression of C_{ant} (*10–15*), ocean interior acidification (OIA) signals penetrate by now several hundred to thousands of meters deep into the ocean, with rates of change that in some regions exceed those at the surface (*16–18*). This subsurface amplification is caused by naturally acidified conditions in the ocean interior due the accumulation of remineralized DIC, which results in a higher sensitivity of some CO_2 system parameters to a given change in DIC (*16*, *17*). Acidification in the ocean interior is of particular concern, because it is home to many OA-sensitive organisms, such as pteropods (*19*, *20*) or the highly diverse organisms inhabiting the sea floor, including cold water corals (*21*, *22*). In fact, it has been speculated that some of these organisms might be more sensitive to OA than those living at the surface (*23*, *24*).

Yet, our current quantitative understanding of the time-history and progression of ocean interior acidification is not very well developed. This is largely a consequence of the dearth of observations that limit the extension of the surface ocean OA studies to depth. Notable exceptions are local studies based on time series stations (*25–27*) and repeat hydrography sections (*28–35*). All of these studies find acidification rates in the surface mixed layer of the ocean that primarily reflect the rate of increase of atmospheric CO_2 over the observational period, causing a pH decline of ~0.002 yr^{-1} and a reduction of the saturation state of aragonite (Ω_{arag}) by ~0.001 yr^{-1}. Over the forty year extension of the longest time series records, this corresponds to a pH decline approaching 0.1 (equivalent to an H^+ increase of more than 30%) and a drop of Ω_{arag} by >0.3. In some study regions, acidification rates below the mixed layer were found to be more variable than at the surface. This subsurface variability tends to occur along isopycnals (*28*) and to be more pronounced in shorter time series.

Although the main driver of OIA in these studies is the accumulation of C_{ant}, the elevated variability of the interior acidification rates indicates that changes in the ocean's pH or Ω can also occur because of changes in the natural carbon cycle (*3*) altering either the concentration of dissolved inorganic carbon (DIC) or alkalinity (TA) or both (*36*). These changes can be driven by water mass redistributions or changes in the ocean's biological pumps, namely changes in the remineralization of organic matter or changes in the dissolution of mineral calcium carbonate (*37*). Here, we focus exclusively on OIA driven by C_{ant}, and this for three reasons. First, it can be expected that under exponentially growing atmospheric CO_2 and over multi-decadal to centennial timescales, changes in the natural carbon cycle have a lower impact on OA rates compared to the accumulation of C_{ant} (*28*). This is well supported by local attribution studies conducted so far, which suggest that between 60 to 100% of the observed decadal changes in pH and/or Ω at depth

are due to the downward progression and subsequent accumulation of C_{ant}. Second, this focus is consistent with the original coinage of the term "Ocean Acidification", which was indeed meant to reflect only the change in the ocean's chemistry driven by the uptake of anthropogenic CO_2 (*38*). Third, we have global observation-based estimates available of the accumulation of C_{ant} over the period 1800 until 2014 (*13*, *14*), permitting us to reconstruct the history of OIA over the entire industrial period.

This observation-based approach to reconstruct OIA has first been used to estimate the shoaling of the aragonite saturation horizon ($\Omega_{arag} = 1$) along a meridional section through each ocean basin (*39*) from a global scale reconstruction of the C_{ant} accumulation until 1994 (*13*). This study found that the aragonite saturation horizon in the North Atlantic Ocean (20–50°N) remained surprisingly stable since pre-industrial times. However, this conclusion was derived from a single section located in the eastern North Atlantic, where C_{ant} does not penetrate as deep as in the western part of the basin. Similar analysis for multiple repeat hydrography sections in the Pacific indeed found strong spatial gradients in ocean interior acidification rates (*18*). So far, there was no global observation-based reconstruction of OIA trends available to put regional section-based results in a global context and investigate in a consistent way the progression of OIA over the industrial era.

Of course, numerical ocean models can provide spatio-temporally resolved OIA fields and extend observation-based assessments backward and forward in time (*6*, *40*). This potential has been leveraged to demonstrate that surface OA has accelerated rapidly over the recent decades reflecting the exponential growth in atmospheric CO_2 (*40*). However, substantial shortcomings in simulating the marine CO_2 system in the ocean interior (*41*, *42*), leading to strong biases in the local sensitivities to OIA, call for observation-based reconstructions of OIA.

The interior ocean dimension of OA is also not reflected in the planetary boundaries concept that was designed to determine safe operating spaces for humanity (*43*, *44*). The current planetary boundary of OA is based solely on surface ocean conditions. This boundary is not considered as *transgressed* because the global mean surface Ω_{arag} has not yet fallen below 80% of its preindustrial value (*43*, *44*). This boundary was adopted in the planetary boundary studies to represent a situation where high latitude surface waters become undersaturated with respect to aragonite ($\Omega_{arag} < 1$) and coral reef ecosystems start to suffer from Ω_{arag} below 3 – 3.5 (*45*). Thus, this planetary boundary definition does not do justice to the impact of OIA on organisms and ecosystems living beneath the surface.

The aim of this study is to provide a global observation-based history of ocean interior acidification driven by the uptake and accumulation of anthropogenic CO_2 unraveling trends and patterns over the industrial era. We deem this important to (i) provide global context to local OA studies covering the recent past, (ii) establish a reference for the evaluation of ocean models and (iii) inform the assessment of habitat changes for organisms populating the ocean interior. We establish our OIA reconstruction based on three dimensional fields of the accumulation of C_{ant} that have previously been obtained from DIC and other biogeochemical and physical tracers using either the C* method (*13*, *46*) or the eMLRC* method (*14*, *47*). We combine these C_{ant} estimates with modern-day climatologies of the marine CO_2 system, nutrients (*48*), and physical properties of the ocean (*49*, *50*). This synthesized data set allows us to compute the state and evolution of the marine CO_2 system from pre-industrial times (~1800) to the reference years 1994, 2004, and 2014.

Results and Discussion

Global mean history of ocean interior acidification

Our reconstructions of the global mean vertical profiles reveal the distinct history of ocean interior acidification, especially its rapid and accelerating progression deep into the ocean's interior (Fig. 1). In 2014 and in the global mean, the entire water column down to nearly 1500 m is measurably affected by the changes. Our reconstructed changes in surface Ω_{arag} of -0.61 ± 0.01 and surface pH_T of -0.117 ± 0.003 over the industrial period up to 2014 (Table 1) agree well with independent estimates (*40*), reflecting the fact that near-surface C_{ant} and thus pH and Ω_{arag} are very closely following the perturbation in atmospheric CO_2 (*3*, *51*). Even though $\Delta\Omega_{arag}$ and ΔpH_T decrease markedly with depth, the global mean decrease in these two properties from 100 - 500 m still amounts to -0.34 ± 0.02 and -0.094 ± 0.006, respectively (Table 1), reflecting the deep and growing accumulation of anthropogenic CO_2 in the ocean interior (Fig. 1C).

A closer inspection reveals marked differences between the mean vertical profiles of $\Delta\Omega_{arag}$ and those of ΔpH_T and the free proton concentration (ΔH^+) shown in Fig. 1. While the global mean profiles of $\Delta\Omega_{arag}$ (Fig. 1A) closely mirror those of the changes in C_{ant} (Fig. 1C) the global mean profiles of ΔpH_T (Fig. 1F) and ΔH^+ (Fig. 1D) reveal subsurface extrema at around 300 m depth. In 2014, the peak of the subsurface maximum in ΔH^+ (2.22 ± 0.20 nmol kg^{-1}) was about 50% higher than the corresponding change in the surface ocean (1.72 ± 0.13 nmol kg^{-1}). For pH, the subsurface minimum is less strongly expressed, due to the logarithmic scale. These subsurface extrema in ΔpH_T and ΔH^+ were previously attributed to the increasing sensitivity with depth of H^+ (and pH_T) to changes in DIC (*16*), that is, the sensitivity $\Delta H^+/\Delta DIC$ (and $\Delta pH_T/\Delta DIC$) shown in Fig. 1E,G. In the top few hundred meters, these sensitivities increase more rapidly with depth than ΔC_{ant} decreases, leading to the maximum of the total change ($\Delta H^+ \approx \Delta H^+/\Delta DIC \cdot \Delta C_{ant}$) at around 300 m. In contrast, the sensitivity of Ω_{arag} to changes in DIC ($\Delta\Omega_{arag}/\Delta DIC$) decreases gradually with depth. As a consequence, the $\Delta\Omega_{arag}$ profiles are surface intensified compared to those of ΔC_{ant}.

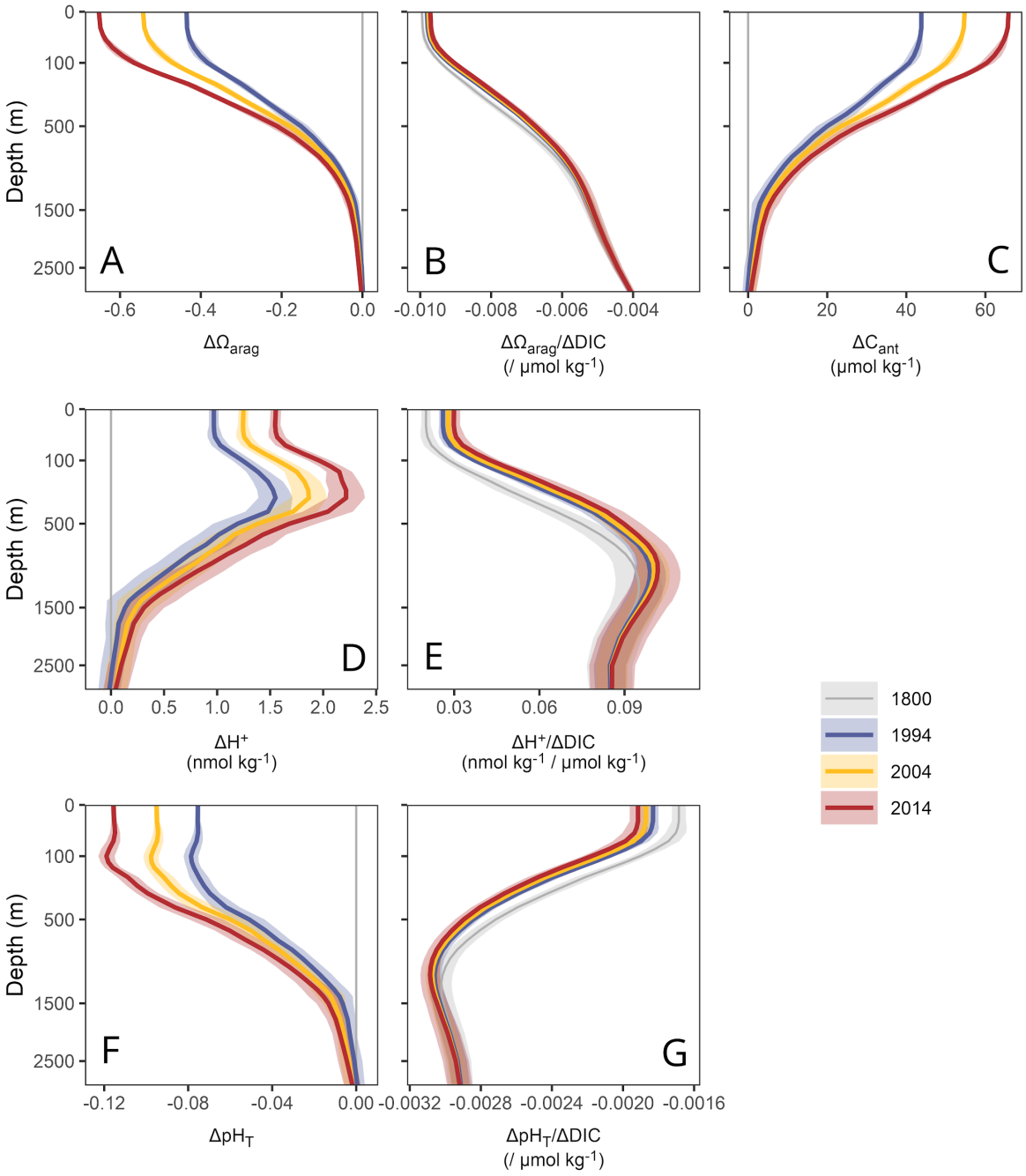

Fig. 1: Global mean vertical profiles of the changes in the marine CO_2 system: Progression of (**A**) changes in the saturation state of aragonite ($\Delta\Omega_{arag}$), (**B**) the local sensitivity of Ω_{arag} to changes in dissolved inorganic carbon ($\Delta\Omega_{arag}/\Delta DIC$), (**C**) changes in the anthropogenic carbon concentration (ΔC_{ant}), (**D**) changes in the free proton concentration (ΔH^+), (**E**) the local sensitivity of H^+ to changes in DIC ($\Delta H^+/\Delta DIC$), (**F**) changes in pH on the total scale (ΔpH_T), and (**G**) the local sensitivity of pH_T to changes in DIC ($\Delta pH_T/\Delta DIC$). Colors distinguish changes since 1800 for the reference years 1994, 2004, and 2014, or the local sensitivities for the respective years.

The acceleration of ocean acidification over the last 20 years is remarkable. Relative to the change that had occurred until 1994, the acidification progressed by around 50% between 1994 and 2014 (Fig. 1, Table 1). This is primarily due to the near exponential growth of atmospheric CO_2, pushing an exponentially growing amount of C_{ant} into the ocean, which then leads to an exponential growth of the accumulated C_{ant} at depth (*12*, *52*). Under the assumption of a steady-state circulation, this tight connection between uptake and transport leads to a steady-state accumulation of C_{ant} across all depths in proportion to the growth in atmospheric CO_2 (*3*). In the

global mean, the reconstructed C_{ant} follows this transient steady-state model quite well (Fig. 1C). This translates also into the ΔH^+, ΔpH_T, and $\Delta\Omega_{arag}$ profiles having nearly proportional changes with depth (Fig. 1, Table 1) with only a few percent deviations from the global mean value. For $\Delta\Omega_{arag}$ this proportional change over time is almost identical with that of C_{ant}, whereas the proportional changes for H^+ and pH_T accelerated due to the increases of the respective sensitivities over time. (Figs. 1, S6).

Table 1: Global mean state, changes and the progression of change in the marine CO_2 system. Results are provided for the saturation state of aragonite (Ω_{arag}), the free proton concentration (H^+ in nmol kg^{-1}), pH on the total scale (pH_T), dissolved inorganic carbon (DIC in µmol kg^{-1}) or the anthropogenic carbon concentration (C_{ant} in µmol kg^{-1}), as well as the mean depth of four isosurfaces of Ω_{arga} (in m). Globally averaged marine surface CO_2 (in ppm) data from NOAA/GML are provided as a reference (*53*). *Progression of change is not reported for the depth layer 1500-3000m, because the change in the C_{ant} is below the detection limit.

		Mean state		Change		Progression
Variable	**Condition**	**1800**	**2014**	**1800-2014**	**1994-2014**	**1994-2014 / 1800-1994**
CO_2	Atmosphere	282.5	395.7	113.2	39.0	52 %
H^+	0 - 100 m	5.55 ± 0.3	7.26 ± 0.4	1.72 ± 0.09	0.64 ± 0.04	59 ± 2 %
Ω_{arag}		3.31 ± 0.1	2.7 ± 0.1	-0.61 ± 0.01	-0.2 ± 0.005	48 ± 1 %
pH_T		8.17 ± 0.02	8.05 ± 0.03	-0.117 ± 0.003	-0.04 ± 0.001	52 ± 1 %
DIC or C_{ant}		2003 ± 10	2066 ± 10	63 ± 1	21 ± 0.5	49 ± 1 %
H^+	100 - 500 m	9.2 ± 0.5	11.24 ± 0.6	2.04 ± 0.2	0.62 ± 0.05	44 ± 3 %
Ω_{arag}		1.87 ± 0.07	1.53 ± 0.07	-0.34 ± 0.02	-0.1 ± 0.004	43 ± 2 %
pH_T		8 ± 0.02	7.9 ± 0.02	-0.094 ± 0.006	-0.029 ± 0.001	43 ± 2 %
DIC or C_{ant}		2135 ± 9	2175 ± 9	40 ± 2	12 ± 0.5	43 ± 2 %
H^+	500 - 1500 m	12.81 ± 0.8	13.58 ± 0.9	0.78 ± 0.2	0.28 ± 0.07	57 ± 14 %
Ω_{arag}		0.98 ± 0.05	0.9 ± 0.05	-0.08 ± 0.009	-0.02 ± 0.003	47 ± 5 %
pH_T		7.85 ± 0.03	7.82 ± 0.03	-0.031 ± 0.005	-0.011 ± 0.002	52 ± 9 %
DIC or C_{ant}		2247 ± 9	2259 ± 9	11 ± 2	4 ± 0.5	49 ± 7 %
H^+	1500 - 3000 m	12.36 ± 0.9	12.49 ± 0.9	0.14 ± 0.1	0.1 ± 0.04	*
Ω_{arag}		0.76 ± 0.05	0.74 ± 0.04	-0.01 ± 0.005	-0.01 ± 0.002	*
pH_T		7.86 ± 0.03	7.86 ± 0.03	-0.006 ± 0.003	-0.004 ± 0.001	*
DIC or C_{ant}		2279 ± 10	2281 ± 10	2 ± 1	1 ± 0.4	*
Mean depth of isosurfaces	$\Omega_{arag} = 1$	939 ± 133	728 ± 127	-222 ± 14	-63 ± 11	43 ± 8 %
	$\Omega_{arag} = 2$	298 ± 15	218 ± 14	-106 ± 4	-34 ± 2	44 ± 4 %
	$\Omega_{arag} = 3$	156 ± 7	101 ± 8	-77 ± 4	-29 ± 2	53 ± 6 %
	$\Omega_{arag} = 4$	73 ± 10	35 ± 15	-72 ± 7	-44 ± 6	57 ± 22 %

Spatial patterns in ocean interior acidification trends

The vertical penetration of $\Delta\Omega_{arag}$, ΔH^+, and ΔpH_T differ strongly between regions (Fig. S2), motivating a more detailed spatial assessment. As was the case for the global mean vertical profile, the spatial distribution of $\Delta\Omega_{arag}$ (Figs. 2 and 4) closely resembles that of ΔC_{ant} (Figs. 4 and S3). Within the top 100 m, the largest changes in Ω_{arag} occurred in the subtropical and equatorial regions, where Ω_{arag} declined by almost one unit over the industrial era until 2014 (Fig.

2B). The decline of Ω_{arag} in the top 100 m is slightly higher in the tropics and subtropics of the Atlantic compared to the Indo-Pacific. This is a result of higher accumulation rates of C_{ant} in the Atlantic, in particular from 1800 - 1994 (*13*), which itself is a consequence of the more favorable buffer factor in the Atlantic, giving it a higher uptake capacity (*51*).

In the subtropical gyres, the isolines of $\Delta\Omega_{arag}$ generally penetrate deeper into the ocean compared to equatorial or high latitude regions (Fig. 4). As a consequence, the mean $\Delta\Omega_{arag}$ over the depth layer 100 - 500 m reveals strong latitudinal gradients, with $\Delta\Omega_{arag}$ in the center of the subtropical gyres (~30° N/S) being about twice as high as in equatorial regions or the high latitudes (Fig. 2E). The exceptionally deep penetration of ΔC_{ant} in the North Atlantic caused a decline of Ω_{arag} by more than 0.1 until 2014 even at 1500-3000 m depth (Figs. 2K and 4), a magnitude of change that is not found anywhere else in this depth layer.

The latitudinal gradients in $\Delta\Omega_{arag}$ vary little over time (Fig. 2, left column), as expected from the near transient steady state development of C_{ant}, which leads to a decrease in $\Delta\Omega_{arag}$ that scales nearly linearly with atmospheric CO_2 (Fig 2, right column). An important exception is the recent decline of the acidification rate in the deep North Atlantic relative to the increase in atmospheric CO_2 (Fig. 2L). This can be attributed to the weak C_{ant} accumulation at depth from 2004 to 2014 (*14*) shown in Fig. S3.

Within the top 100 m, H^+ is reconstructed to have increased the most in the eastern tropical Pacific and eastern tropical Atlantic, largely a consequence of these low pH regions having the highest sensitivity $\Delta H^+/\Delta DIC$ (Fig. S6). Apart from these regions, the highest changes in H^+ occurred in the high latitudes. The subsurface peak in ΔH^+ seen in the global mean profiles (Fig. 1D) stems largely from the equatorial upwelling regions and the North Pacific (Fig. 3). In these regions, the highest H^+ changes occur at around 300 m water depth and exceed 3 nmol kg^{-1} in 2014 (Fig. 4), which is almost twice as high as the global mean change in the surface layer (1.72 ± 0.13 nmol kg^{-1}). Subsurface maxima in ΔH^+ are also widespread in the subtropical gyres. Subsurface maxima in the subtropics are not as intense as in the upwelling regions (Fig. 4), but occur several hundred meters deeper in the water column (Fig. S11). Below ~1000 m, the spatial pattern in ΔH^+ is very similar to that of $\Delta\Omega_{arag}$ in that substantial changes are only found in the North Atlantic (Fig. 4).

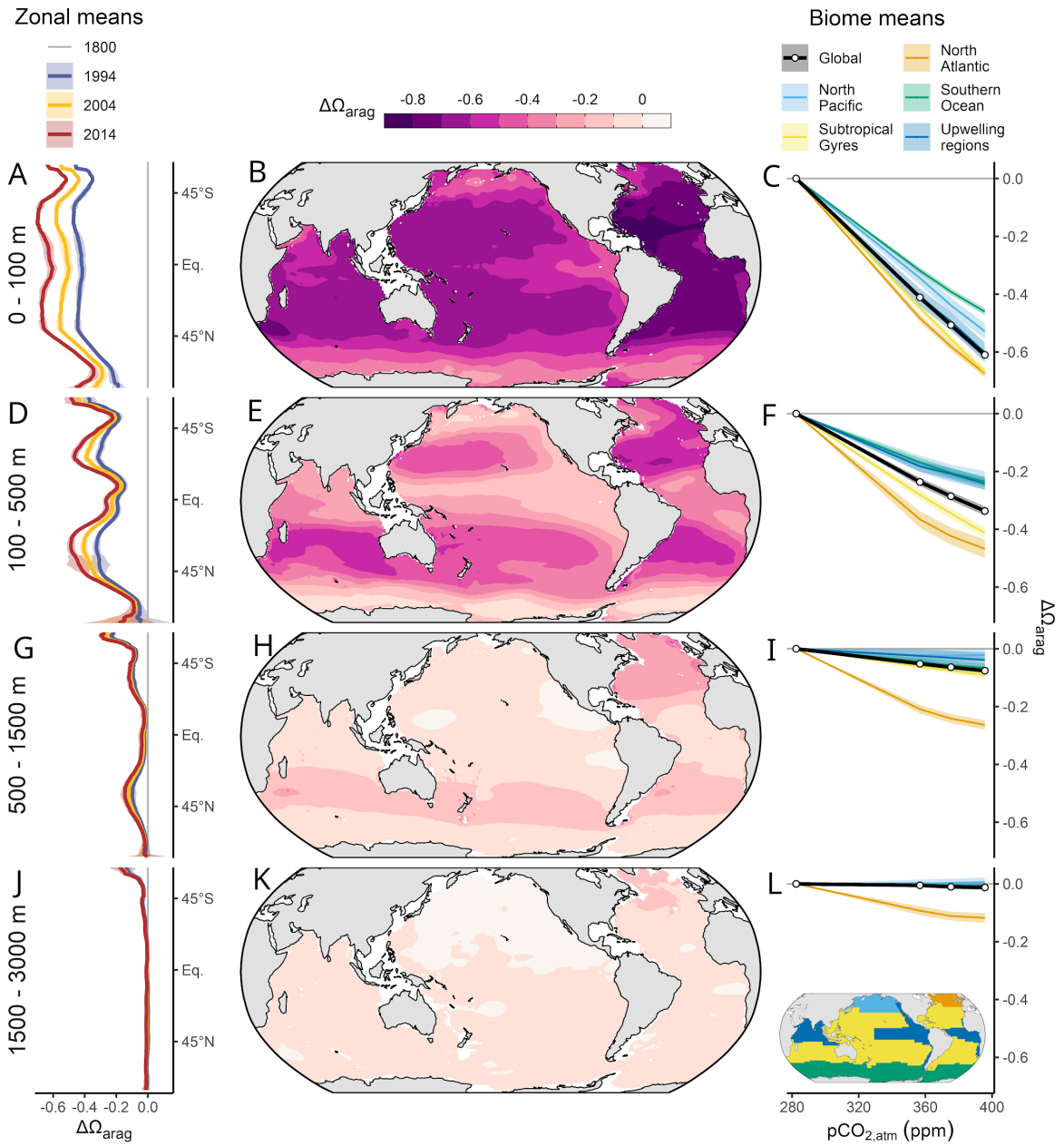

Fig. 2: Spatial patterns in the changes of the saturation state of aragonite ($\Delta\Omega_{arag}$). Acidification trends are averaged over four depth layers (panel rows), that is 0 m to 100 m, 100 m to 500 m, 500 m to 1500 m, and 1500 m to 3000 m. Central panels (**B,E,H,K**) show maps of $\Delta\Omega_{arag}$ from 1800 - 2014. The corresponding zonal mean distributions of $\Delta\Omega_{arag}$ in the left panels (**A,D,G,J**) display changes since 1800 for the three reference years 1994, 2004 and 2014. Right panels (**C,F,I,L**) show mean $\Delta\Omega_{arag}$ averaged over the regions shown on the inset map (L) and plotted as a function of the increase in atmospheric CO_2.

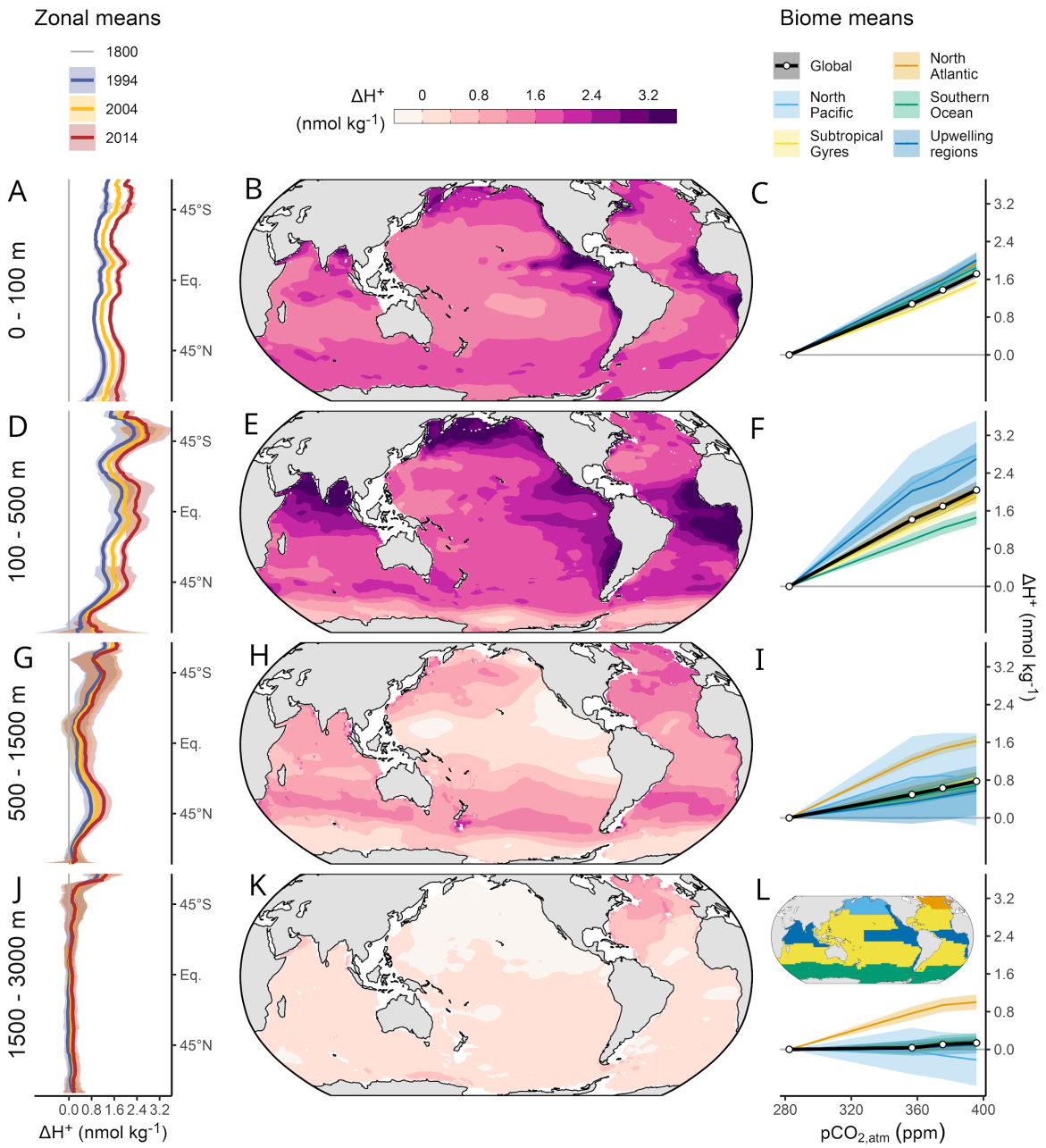

Fig. 3: Spatial patterns in the changes of the free proton concentration (ΔH^+). Figure formatting is otherwise consistent with Fig. 2.

As was the case for $\Delta\Omega_{arag,}$ the latitudinal gradients of ΔH^+ changed little over time (Fig. 3, left column). More difference emerges when the changes are plotted versus the increase in atmospheric CO_2 (Fig. 3, right column). Consistent with the near transient steady state development of C_{ant}, ΔH^+ tends to increase in proportion to the increase in atmospheric CO_2, but deviations in the rate of OIA that are larger than for $\Delta\Omega_{arag}$ become evident in upwelling regions, the North Pacific, and the North Atlantic. These deviations are related to higher changes in the sensitivity $\Delta H^+/\Delta DIC$ over time (Fig. S6), which amplifies the temporal variability in ΔC_{ant} (Fig. S3).

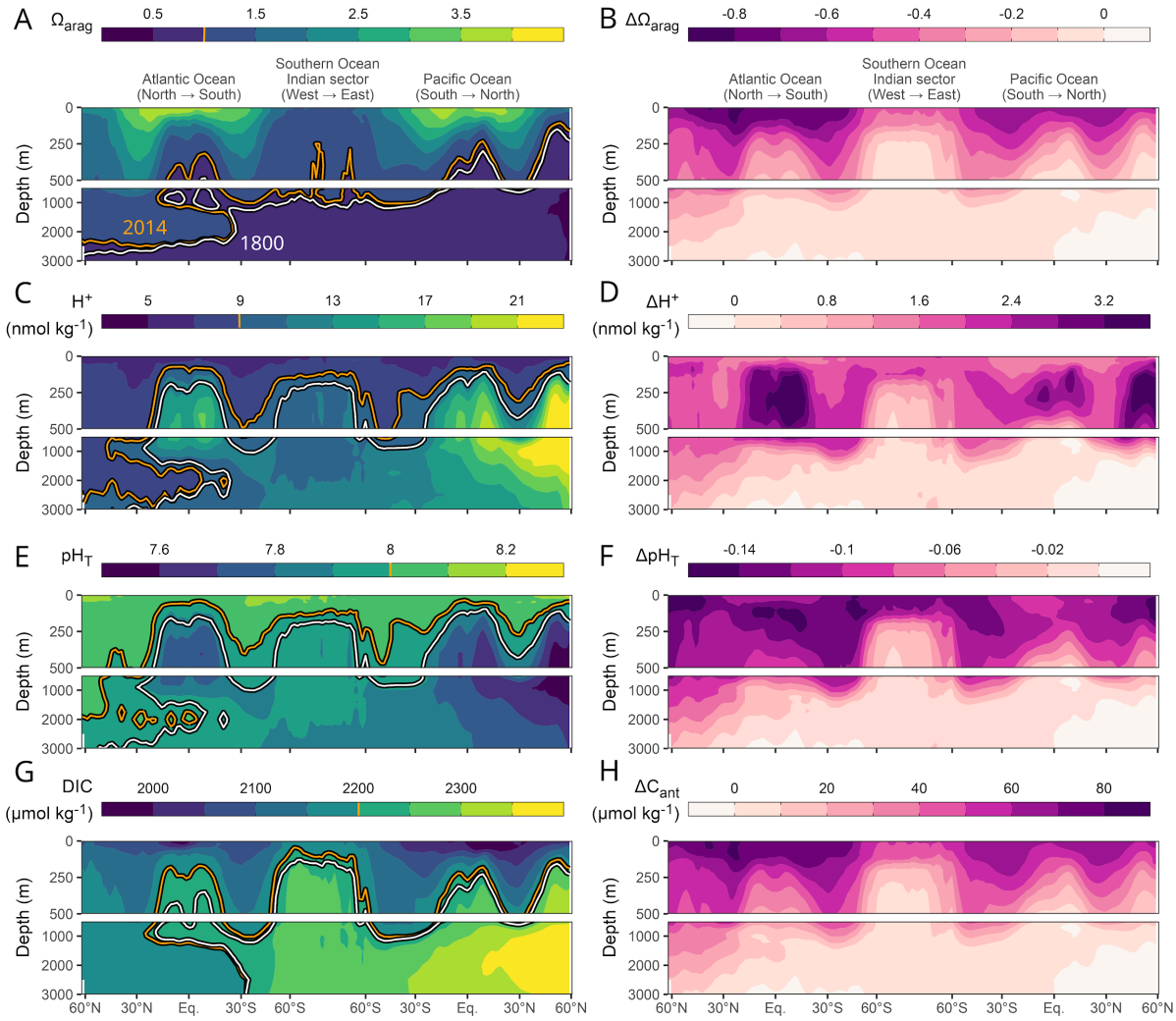

Fig. 4: Global mean sections of the absolute state of the marine CO_2 system in 2014 (left panels) and changes from 1800 to 2014 (right panels). Panel rows distinguish the saturation state of aragonite (Ω_{arag}; **A,B**), the free proton concentration (H^+; **C,D**), pH on the total scale (pH_T; **E,F**) and the anthropogenic carbon concentration (C_{ant}; **G,H**). Contour lines on the left panels indicate absolute levels of $\Omega_{arag} = 1$, $H^+ = 9$ nmol kg^{-1}, $pH_T = 8$, and DIC = 2200 µmol kg^{-1} in 2014 (orange) and 1800 (white).

In summary, the spatial patterns in OIA acidification trends are a direct consequence of the accumulation of C_{ant} and the local sensitivities of the CO_2 system (Fig. S5, S6, S10). These sensitivities are generally high when the absolute values of Ω_{arag} and H^+ are high (Figs. 4, S8, S16). To first order, these background conditions are determined by the accumulated amount of remineralized DIC, which decreases/increases Ω_{arag}/H^+, respectively. This prominent role of remineralized DIC in controlling ocean interior acidification rates has previously been investigated in detail (*16*, *17*), albeit without considering the progression of OIA beyond 2002.

Acidification of the seafloor and integrated across water masses

A region of special concern for OIA is the seafloor, of which we consider here only that portion that is shallower than 500 m and most strongly impacted by OIA (Fig. 4). As displayed in Fig. 5a, we find that the proportion of the seafloor that experienced a decline in Ω_{arag} by more than 0.5 quadrupled over the two most recent decades of our reconstruction from 11 ± 0 % in 1994 to 47 ± 4 % in 2014. The strongest reduction in the affected seafloor fraction occurred in the $\Delta\Omega_{arag}$ interval -0.3 to -0.4, from ~30 % in 1994 to roughly 10 % in 2014. The most common $\Delta\Omega_{arag}$

interval in 2014 was -0.5 to -0.6, while it was -0.3 to -0.4 in 1994. These Ω_{arag} changes along the seafloor are largely mirrored by the Ω_{arag} changes in the volume fractions over the top 500 m (Fig 5b). For example, the ocean volume affected by a decline in Ω_{arag} by more than 0.5 increased from <5 % to 35 ± 1 %. The primary driver for the distribution of the changes in Ω_{arag} is the change in C_{ant} (Fig 5E,F)

Like for Ω_{arag}, we find a strong increase of the seafloor (and volume) fractions that are affected by high changes in H^+ (Fig 5B,C). The fractions that experienced $\Delta H^+ >= 2.0$ nmol kg^{-1} (roughly equivalent to $\Delta pH_T < -0.1$) grew from 16 ± 3% (and 14 ± 1%) in 1994 to 42 ± 8% (and 37 ± 5%) in 2014. The strongest corresponding reduction in affected seafloor and volume fractions was identified in the ΔH^+ interval 0.8 - 1.2 nmol kg^{-1}. Below, we will discuss how acidification at the seafloor affects the conditions at known locations of cold water corals.

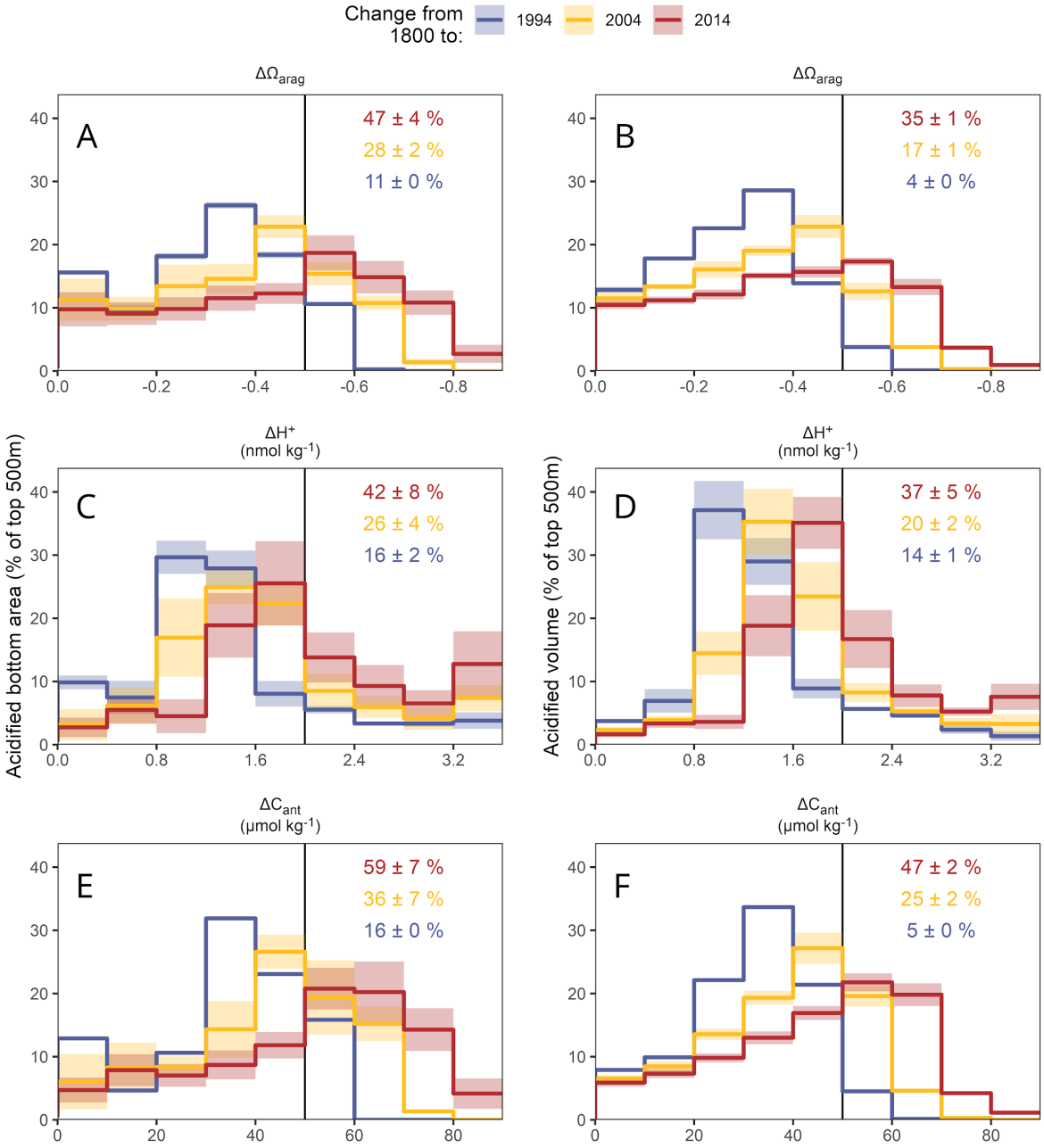

Fig. 5: Acidified seafloor (left panels) and volume (right panels) fractions of the ocean. Estimates are determined over the top 500 m of the ocean for intervals of changes in (**A,B**) the saturation state of aragonite ($\Delta\Omega_{arag}$), (**C,D**) the free proton concentration (ΔH^+), and (**E,F**) the anthropogenic carbon concentration (ΔC_{ant}). Coloured lines distinguish fractions for 1994, 2004 and 2014, with ribbons indicating ranges of uncertainty.

The shoaling of the saturation horizon and the loss of saturated waters

Further insight into the progression of OIA can be obtained by looking at the shoaling of the saturation horizon and that of the depths of various other isosurfaces of Ω_{arag} (Figs. 4, 6) as well as the corresponding volume loss of waters above these Ω_{arag} thresholds (Fig. 7). In consistency with previous studies, we restrict this analysis to the top 3000 m of the ocean to avoid reconstruction uncertainties of ΔC_{ant} in the deep ocean (*14*, *54*). Hence, relative volume changes are referenced to the total ocean volume above this depth.

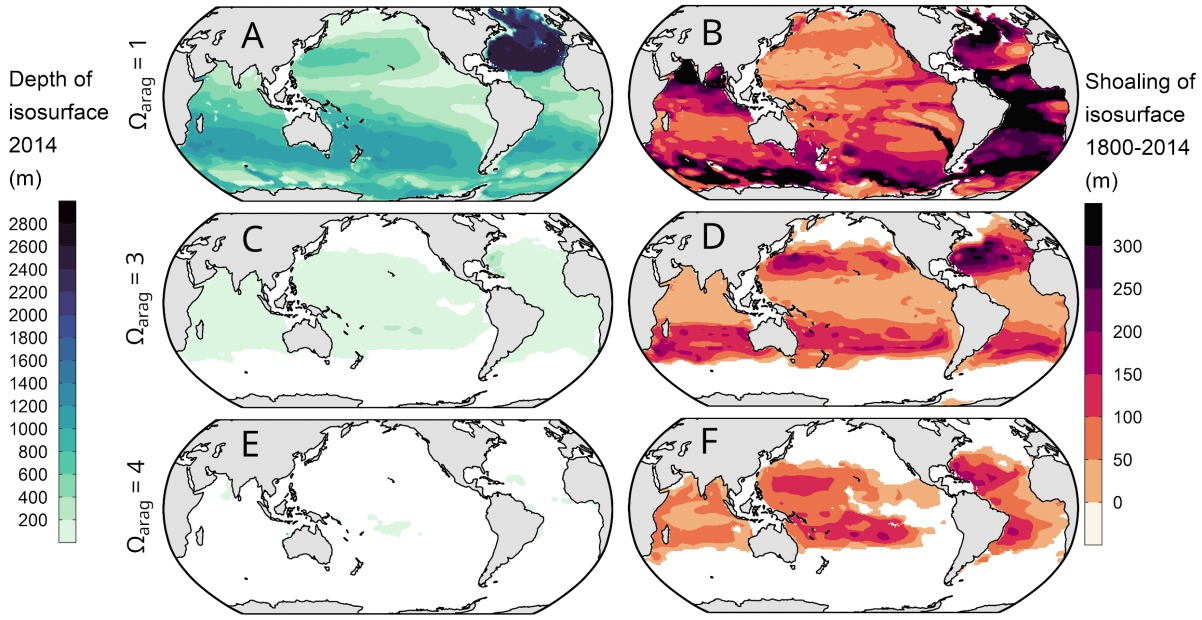

Fig. 6: Isosurfaces of the saturation state of aragonite (Ω_{arag}) in 2014 (left panels) and their shoaling from 1800 - 2014 (right panels). Displayed are the isosurfaces for the saturation states 1 (**A,B**), 3 (**C,D**), and 4 (**E,F**).

An illustrative example is the shoaling of the isosurface Ω_{arag}=4, which is considered a threshold for optimal growth of warm water corals (*55*). Back in 1800 this isosurface still existed throughout most parts of the tropical ocean between 30° N and 30°S (Fig. 6) but by 2014, it had surfaced in most regions of the world ocean except for very small remaining patches in the tropics. This near complete disappearance of waters with a mean Ω_{arag} >= 4 from the global ocean is consistent with independent assessments of changes of Ω_{arag} at the ocean surface (*40*). However, temporarily and locally water masses may still experience Ω_{arag} >= 4, for example, due to the seasonal elevation of the saturation state through primary production. The fate of water masses with Ω_{arag} above 3, which is considered as marginal to inadequate for coral growth (*55*), has followed a similar trajectory as those for the Ω_{arag} = 4 threshold. The mean depth of the isosurface Ω_{arag} = 3 shoaled over the industrial period by 77 ± 4 m to 101 ± 8 m in 2014 (Table 1, Fig. 6), leading to a 40% reduction of the preindustrial volume of waters with Ω_{arag} > 3 (Fig. 7). Interestingly, the surface area of the ocean maintaining Ω_{arag} > 3 reduced only by about 20% over the industrial and is hence not strongly correlated to the shoaling of the corresponding isosurface and volume loss, suggesting that the remaining surface area of saturated conditions is a weak (or at least incomplete) indicator of the progression of OA in the ocean's interior.

The isosurface of Ω_{arag} = 1, commonly referred to as the saturation horizon, which separates waters supersaturated in aragonite above it from undersaturated waters below it, shoaled from 940 ± 133 m in 1800 to 728 ± 127 m in 2014 (Table 1). This corresponds to a global average shoaling by 222 ± 14 m over the industrial era. This shoaling caused a loss of saturated water masses of 6.3 ± 0.5% of the top 3000m ocean volume (Fig. 7), corresponding to a loss of about 20% of the pre-industrial volume with Ω_{arag} >= 1. This is expected to have strong impacts on global biogeochemical cycles by increasing the volume of water masses that are corrosive for aragonite and hence favour the dissolution of particulate inorganic carbon (*39*).

The shoaling of these isosurfaces and the history of the loss of waters above a certain Ω_{arag} tends to scale rather linearly with the increase in atmospheric CO_2 and the accumulation of

anthropogenic CO_2 in the ocean (Fig 7). For example, the shoaling of the $\Omega_{arag} = 3$ isosurface of about 80 m occurred in response to atmospheric CO_2 going up by 107 ppm, yielding a proportionality of ~0.7 m ppm^{-1} (Figure 7). Hence, the current growth rate of atmospheric CO_2 of around 2 ppm yr^{-1} causes an additional shoaling of this isosurface by 1.4 m yr^{-1}. The global mean saturation horizon of aragonite ($\Omega_{arag} = 1$) shoals currently by 4.2 m yr^{-1}, corresponding to the loss of an additional 1.5% of supersaturated water masses per decade.

While the saturation horizon shoals globally relatively slowly and is still rather deep, the situation is very different in the Southern Ocean. Here, the shoaling of the saturation horizon over the industrial era is among the highest across the globe, amounting to nearly 300 m, on average (Fig. 6). The reason for this pronounced shoaling are the generally weak vertical gradients in the saturation state for $\Omega_{arag} \approx 1$ in the Southern Ocean (Fig. S12), such that a small change in Ω_{arag} can induce a strong uplift of the saturation horizon (*56*). An even larger shoaling occurred in the regions with the shallowest 10% depth of the saturation horizon. There, the saturation horizon migrated upward over the industrial period by more than 700 m, reaching by 2014 a mean depth of 250 ± 336 m. Hence, the surface layer of the Southern Ocean is primed to locally experience already now corrosive conditions with respect to aragonite, putting its sensitive organisms at risk (*56*, *57*).

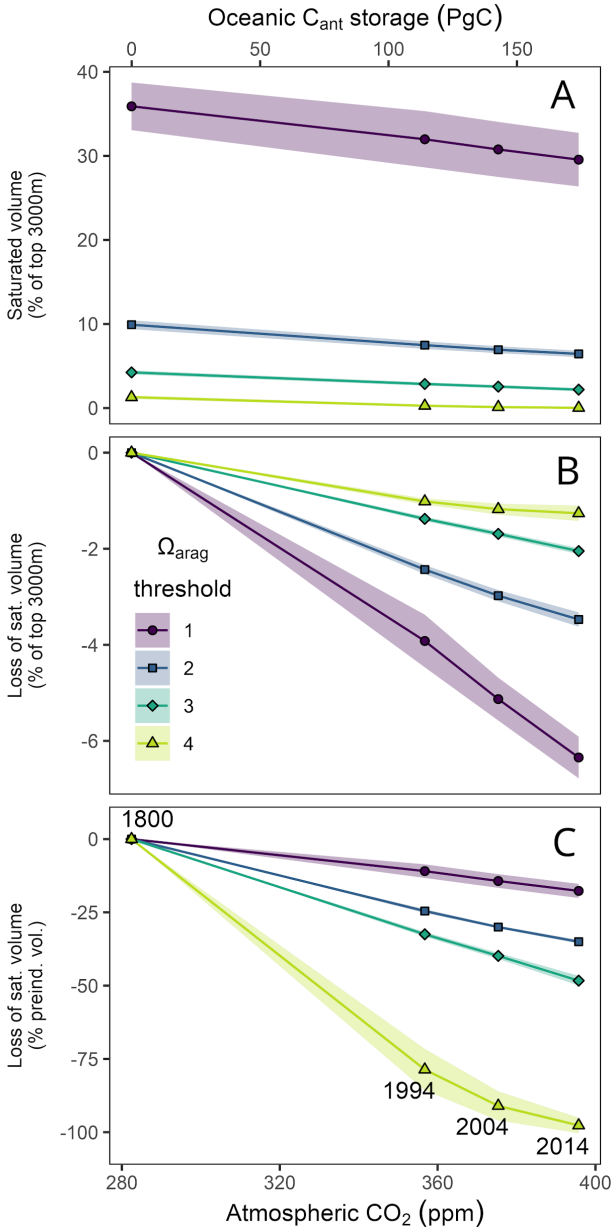

Fig. 7: Changes in ocean volumes supersaturated with respect to aragonite for four saturation thresholds (1, 2, 3, and 4). Volume changes are displayed as a function of atmospheric CO_2 (bottom x-axis) and the globally integrated oceanic storage of anthropogenic carbon (C_{ant}). Volumes are integrated over top 3000 m and displayed as (**A**) the relative fraction of the volume of the upper 3000 m of the ocean, (**B**) the corresponding volume loss, and (**C**) the volume loss relative to the saturated volume in pre-industrial times.

Impact on two groups of ecologically relevant marine organisms

We contextualize our reconstructed history of OIA further by illustrating its potential impact on cold water corals and pteropods, two ecologically important groups of organisms that inhabit the ocean interior and are widely dispersed around the globe.

First, we investigate the progression of OIA at known locations of cold water corals. Their reefs form biodiversity hotspots along the edges of continental shelves and seamounts (*21*), and occur down to depths of several hundreds of meters (Fig. 8A). Here, we rely on an updated database for the global distribution of cold water corals (*58*), from which we obtained 326 unique locations of six species (*Lophelia pertusa*, *Madrepora oculata*, *Goniocorella dumosa*, *Oculina varicosa*, *Enallopsammia profunda*, *Solenosmilia variabilis*; following (*22*)) within our study domain. We find that 8% of these locations occurred in undersaturated conditions around 1800 (Fig. 8D), broadly consistent with previous results (*22*). By 2014, this exposure almost doubled to 14%. In addition, the fraction of cold water coral living in conditions characterized by $\Omega_{arag} < 2$ increased from 63% to 92% over the industrial period. As a consequence, the range of Ω_{arag} conditions shifted downward and compressed by about 30% over the industrial period (Fig. 8D), expressed in a decline of the interquartile range from ~0.9 in 1800 to ~0.6 in 2014. This compression of Ω_{arag} conditions has been identified before in a modeling study (*59*), and bears the potential of a rather sudden transgression of large fraction of cold water coral locations into undersaturated conditions. Importantly, OIA will continue to progress even under the hypothetical scenario that CO_2 emissions immediately decline to zero, because of the interior redistribution of anthropogenic carbon that is already stored in the upper ocean. For example, it is predicted that the volume loss of supersaturated waters will progress for another two centuries after carbon emissions stop (*60*). This acidification in the pipeline may eventually expose cold water corals to corrosive conditions, even at locations that currently provide $\Omega_{arag} > 1$.

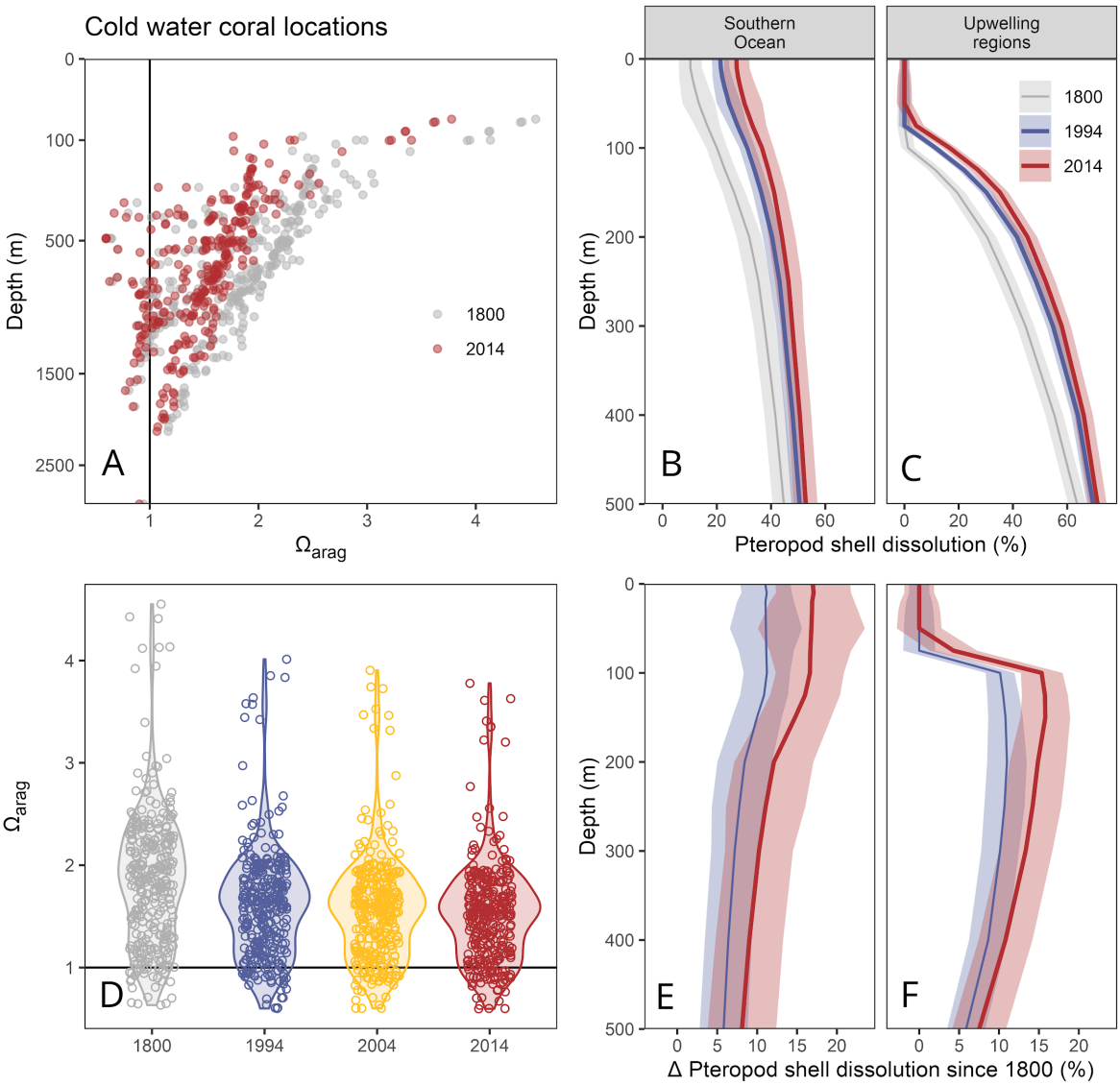

Fig. 8: Impact of ocean interior acidification on benthic (cold water corals) and pelagic (pteropods) organisms. Left panels (**A,D**) show the saturation state of aragonite (Ω_{arag}) at known locations of cold water corals, following a previous model-based assessment (*22*) but building on updated occurrence data (*58*). Right panels show (**B,C**) the vertical distribution of shell dissolution in pteropods for the Southern Ocean and Upwelling Regions, as well as (**E,F**) its increase since 1800. Shell dissolution is estimated from our Ω_{arag} reconstructions (Fig. S12) based on an empirical relationship (*20*), and expressed in percent of pteropod individuals with severe shell dissolution.

Secondly, we estimate the impact of OIA on the degree of shell dissolution in pteropods. These zooplanktonic pelagic calcifiers form an important part of the food web and drive a significant fraction of the global carbonate export through sinking of their aragonite shells (*61*). Pteropods are susceptible to OA in the ocean interior, because the organisms migrate vertically up to several hundred meters (*62*). Our assessment relies on an empirical relationship between the fraction of pteropods affected by severe shell dissolution and environmental Ω_{arag} (*19*, *20*). Applying this relationship (shell dissolution = $-66.29 \times \ln(\Omega_{ar}) + 61.2$) to our reconstructions of Ω_{arag} (Fig. S12), we find distinct regional differences in the estimated shell dissolution and its change over time. In the Southern Ocean, the entire top 500 m of the water column were already favorable for pteropod shell dissolution in preindustrial times, with a vertical gradient from around 10% shell dissolution near the surface to 40% at 500 m. The potential for shell dissolution increased by around 10-20%

over the industrial era with only a weak gradient across depth, although the reduction in Ω_{arag} is strongly surface intensified. This difference in the vertical gradient is a consequence of the higher sensitivity of the shell dissolution on Ω_{arag} at depth, where Ω_{arag} is naturally lower. Averaged over the upwelling regions defined in our study (Fig. 2L), we find that surface Ω_{arag} remained sufficiently high to prevent shell dissolution throughout the industrial era (Fig. 8C). However, low background Ω_{arag} conditions below 100 m are strongly favourable for shell dissolution. Similar to the subsurface maxima in ΔH^+ (Fig. S2), the shell dissolution in these naturally acidified conditions increases strongly over time (Fig. 8F).
Our results indicate that the conditions for the shell formation of pteropods deteriorated over the industrial era. However, the magnitude of this deterioration is highly region-specific, and the exact relationship between the changing variable of the marine CO_2 system (Ω_{arag}) and the biological response (shell dissolution) plays an important role in mediating the impact of ocean interior acidification. In this regard, we caveat that the empirical relationship between Ω_{arag} and shell dissolution that we applied globally has been determined from regional samples collected on the continental shelf off the west coast of North America, where severe shell dissolution was mostly observed in nearshore samples affected by upwelling of corrosive waters. It remains to be tested to which degree this relationship holds in other regions. Hence, our global extrapolation should be considered as an assessment of the potential for shell dissolution, rather than an accurate representation of it.

Caveats and limitations

The most important caveat regarding our estimates of ocean interior acidification trends is their reconstruction solely based on the accumulation of anthropogenic carbon. The reconstructed ΔC_{ant} do not resolve local or regional changes caused by heaving or redistribution of water masses. And the reconstructed changes in Ω_{arag} and H+ do not include the potential contribution of changes in DIC and TA caused by changes in the natural carbon cycle.

Despite this caveat, our surface ocean acidification trends (Figs. 1-3) agree remarkably well with previous estimates based on an ensemble of 14 ESMs that were offset-adjusted to match observation-based patterns in SST, SSS, DIC, and TA (*40*). The model-based global mean increase of H^+ by ~30% (from 6.5 to 8.5 nmol kg^{-1}) from 1750 to 2010 is slightly higher than our estimate (+1.72 ± 0.13 nmol kg^{-1}) due to their coverage of high OA trends in the Arctic. The good agreement of these two independent reconstructions confirms that the accumulation of C_{ant} is indeed the prime driver for surface OA trends over the industrial era. Comparing our estimates to an entirely observation-based reconstruction of the global surface ocean acidification over the past four decades (*51*), we find good agreement in the global mean trends when those are expressed relative to the increase in atmospheric CO_2. However, an interesting difference is that at the ocean surface slightly higher rates of change were observed in the equatorial regions of the Pacific compared to the Atlantic, whereas we find the opposite (Figs. 2, 3). This difference can most likely be attributed to positive surface ΔC_{nat} (*51*) in the Pacific from 1982 to 2021, due to La-Nina conditions (low SST, high DIC) towards the end of the period of the surface study.

More importantly, our ocean interior acidification trends are also overall consistent with direct observation-based estimates. For example, repeated pH measurements conducted in 2006 and 1991 along a meridional section in the North Pacific (P16N) revealed a shoaling of the isocline that marks C_{ant}-driven pH changes of -0.01 from around 600 m at 30°N to 200 m at 50°N (*28*). This latitudinal distribution is well represented in our reconstruction (Fig. S4). However, it was also found that around this isocline, pH changes driven by C_{nat} variability dominated the observed acidification. Similar variability of pH changes around the secular trend driven by the

accumulation of anthropogenic carbon was also observed from repeat hydrography sections in the Atlantic (*35*) and at time series stations (*25*, *26*). It is exactly this type of variability on local to regional and interannual to decadal time scales that our global C_{ant}-based reconstruction can not resolve.

Summary and Outlook

In this study we provide a global reconstruction of the progression of C_{ant}-driven acidification in the ocean interior over the industrial era. We highlight that the OIA patterns differ substantially among acidification parameters, suggesting that OA impact studies should distinguish between these parameters and their absolute vs. relative changes. Over the last two decades of our reconstruction (1994 - 2014), the relative progress of OIA was very even across depth, with an amplification of the acidification signal by about 50% compared to the level already reached in 1994. This leads to a state of OIA in 2014 that we consider critical with respect to regional crossings of important thresholds in the ocean interior, such as a decline of the saturation state of aragonite below 3 or 1. We exemplified the potential impact of OIA over the industrial era on two groups of environmentally relevant organisms: While we inferred a substantial elevation of pteropod shell dissolution, the exposure of cold water coral locations to undersaturated conditions doubled but remained at a low level. However, we know that ocean interior acidification has — in contrast to surface OA — a long-term commitment, that is, OIA will progress for at least 200 years after emissions peak (*55*, *60*) due to the redistribution of already accumulated C_{ant} in the ocean interior. Hence, our results indicate that human CO_2 emissions have already put ecosystems in danger that thrive hundreds or thousands of meters beneath the ocean surface.

We caveat that our reconstructions do not resolve OIA driven by variability in the natural carbon cycle or other environmental drivers such as temperature. Through a comparison to previous, directly observation-based studies, we highlight that neglecting these changes is critical at local to regional and interannual to decadal time scales. Hence, we consider it an important next step to distinguish drivers of OIA more scrupulously by resolving C_{ant}- and natural carbon cycle-driven changes at global scale. A prerequisite for this endeavor is the availability of all required time-resolved ocean interior forcing fields. While DIC (*63*) and temperature (*64*) reconstructions are already available, we recommend prioritizing the development of a similar product for alkalinity to achieve this goal.

Material and Methods

Computation of trends and sensitivities of CO_2 system variables based on storage changes in anthropogenic carbon

We estimate ocean interior acidification (OIA) trends based on reconstructions of the anthropogenic carbon accumulation (ΔC_{ant}) over the industrial era, which we combine with a present day DIC climatology to infer the ocean interior DIC distribution at four reference years (t_{ref}). Specifically, we determined DIC for 1994 and 2004 by adding/subtracting proportional fractions of ΔC_{ant} for the period 1994–2004 (*14*) to/from the DIC climatology centered on the year 2002 (*48*), that is, $DIC(t_{ref}) = DIC(2002) + (t_{ref} - 2002) * \Delta C_{ant,1994–2004}$. Furthermore, we obtained DIC in 1800 by subtracting ΔC_{ant} for the period 1800–1994 (*13*) from DIC in 1994. Likewise, we added ΔC_{ant} for the period 2004–2014 to DIC in 2004 to obtain DIC in 2014.

Based on the four derived DIC climatologies for the reference years 1800, 1994, 2004 and 2014, we calculated the corresponding ocean interior distributions of marine CO_2 system variables using the climatologies of salinity and temperature from the World Ocean Atlas 2018 (*49*, *50*), as well as alkalinity (TA), silicate and phosphate from the gridded GLODAP climatology (*48*). All CO_2 system calculations were done with the R-package seacarb (*65*) using the CO_2 dissociation constants updated for cold waters (*66*) in combination with the fluoride association constant (*67*) and the acidity constant of hydrogen sulfide (*68*). OIA trends were obtained for all CO_2 system variables by subtracting the value in 1800 from those in 1994, 2004 and 2014.

Our approach to reconstruct OIA trends resolves - by definition - the perturbation of the marine CO_2 system by the accumulation of anthropogenic carbon and assumes time-invariant ocean physics through its projection on a fixed density climatology. Hence, changes in the marine CO_2 system that might locally be induced by changes in biogeochemical processes and their interplay with water mass transport are not resolved. In the section “Caveats and limitations” we discuss the role of neglecting these processes.

For the interpretation and attribution of the OIA trends we report the sensitivity of the marine CO_2 system parameters to a DIC perturbation of 1 µmol kg^{-1}. We refer to these sensitivities as $\Delta\Omega_{arag}/\Delta DIC$ and $\Delta H^+/\Delta DIC$. In contrast to the corresponding sensitivities (βDIC and ωDIC) that were previously defined (*69*), we report sensitivities in absolute and not in relative terms.

Definition of ocean regions and depth layers

We aggregate our OIA trends in the horizontal dimension based on Longhurst ocean provinces (*70*), which we combine into five large ocean regions (Figs. 2L, S17) that match primary global patterns in our OIA trends. We further average acidification trends over distinct depth layers with boundaries at 100, 500, 1500, and 3000 m water depth.

Determination of uncertainty

We consider two main contributions to the uncertainty of our ocean interior acidification and sensitivity estimates: (i) The uncertainty associated with the observation-based reconstructions of the C_{ant} accumulation and (ii) the uncertainty of the modern-day climatologies of DIC and TA.

To determine (i), the uncertainty contribution from the observation-based reconstructions of the C_{ant} accumulation, we adapt the same procedure developed for the C_{ant} reconstruction itself (*14*). This approach relies on an ensemble of 10 ΔC_{ant} reconstructions for 1994–2004 and 2004–2014

that were obtained based on modified configurations of the eMLR(C*) method. The members of this ensemble capture the uncertainty of the ΔC_{ant} estimates related to data coverage and quality, the regional clustering of the observations and other methodological aspects. For each ΔC_{ant} ensemble member, we computed the state of CO_2 system individually for the reference years 1994, 2004 and 2014. Following the procedure developed for the C_{ant} reconstruction (*14*), we determine the C_{ant}-induced uncertainty in the change of any CO_2 system variable as the root of the sum of squares (RSS) of the differences between a standard case and the other 9 ensemble members. For this purpose, we use the same standard case reconstruction of ΔC_{ant} and otherwise identical procedures as developed for the C_{ant} reconstruction (*14*), except for excluding one ensemble member that considers non-anthropogenic carbon concentration trends at the surface. Lacking a similar ensemble of reconstructions to derive a spatially resolved C_{ant}-induced uncertainty for the period 1800–1994, we assume that these uncertainties are twice those of the 1994–2014 period, reflecting a factor of two between the global mean surface ΔC_{ant} of the two periods. For acidification estimates, the C_{ant}-reconstruction uncertainties of each period are combined forward in time as the cumulative RSS, reflecting the increase of the uncertainty in the total change over time. Uncertainties for volumetric analysis are not accumulated over time. For sensitivity estimates, the C_{ant}-reconstruction uncertainties of each period are combined forward in time as the cumulative RSS for reference years after 2002 (the reference year of the DIC/TA climatology), and backward in time for years prior 2002.

To determine (ii), the uncertainty contribution from modern-day climatologies of DIC and TA, we computed the CO_2 system from modified fields of these climatologies. Specifically, we increased/decreased the values of DIC by the corresponding mapping errors (up to ~50 μmol kg^{-1}) provided together with the climatologies (*48*). We determined the uncertainty contribution as the mean offset from the reconstruction with the original DIC/TA climatology.

The uncertainty components (i) and (ii) were combined as the RSS of the two individual contributions, and reported along with the trends in the CO_2 system variables obtained from the standard case reconstruction of ΔC_{ant} and the original modern-day DIC/TA climatologies.

References

1. P. Friedlingstein, M. O'Sullivan, M. W. Jones, R. M. Andrew, L. Gregor, J. Hauck, C. Le Quéré, I. T. Luijkx, A. Olsen, G. P. Peters, W. Peters, J. Pongratz, C. Schwingshackl, S. Sitch, J. G. Canadell, P. Ciais, R. B. Jackson, S. R. Alin, R. Alkama, A. Arneth, V. K. Arora, N. R. Bates, M. Becker, N. Bellouin, H. C. Bittig, L. Bopp, F. Chevallier, L. P. Chini, M. Cronin, W. Evans, S. Falk, R. A. Feely, T. Gasser, M. Gehlen, T. Gkritzalis, L. Gloege, G. Grassi, N. Gruber, Ö. Gürses, I. Harris, M. Hefner, R. A. Houghton, G. C. Hurtt, Y. Iida, T. Ilyina, A. K. Jain, A. Jersild, K. Kadono, E. Kato, D. Kennedy, K. Klein Goldewijk, J. Knauer, J. I. Korsbakken, P. Landschützer, N. Lefèvre, K. Lindsay, J. Liu, Z. Liu, G. Marland, N. Mayot, M. J. McGrath, N. Metzl, N. M. Monacci, D. R. Munro, S.-I. Nakaoka, Y. Niwa, K. O'Brien, T. Ono, P. I. Palmer, N. Pan, D. Pierrot, K. Pocock, B. Poulter, L. Resplandy, E. Robertson, C. Rödenbeck, C. Rodriguez, T. M. Rosan, J. Schwinger, R. Séférian, J. D. Shutler, I. Skjelvan, T. Steinhoff, Q. Sun, A. J. Sutton, C. Sweeney, S. Takao, T. Tanhua, P. P. Tans, X. Tian, H. Tian, B. Tilbrook, H. Tsujino, F. Tubiello, G. R. van der Werf, A. P. Walker, R. Wanninkhof, C. Whitehead, A. Willstrand Wranne, R. Wright, W. Yuan, C. Yue, X. Yue, S. Zaehle, J. Zeng, B. Zheng, Global Carbon Budget 2022. *Earth Syst. Sci. Data* **14**, 4811–4900 (2022).
2. T. DeVries, Yamamoto, Kana, R. Wanninkhof, N. Gruber, J. Hauck, J. D. Müller, "Magnitude, trends, and variability of the global ocean carbon sink from 1985-2018" (in review, Global Biogeochemical Cycles, 2023).
3. N. Gruber, D. C. E. Bakker, T. DeVries, L. Gregor, J. Hauck, P. Landschützer, G. A. McKinley, J. D. Müller, Trends and variability in the ocean carbon sink. *Nat. Rev. Earth Environ.*, 1–16 (2023).
4. S. C. Doney, V. J. Fabry, R. A. Feely, J. A. Kleypas, Ocean Acidification: The Other CO2 Problem. *Annu. Rev. Mar. Sci.* **1**, 169–192 (2009).
5. J. C. Orr, V. J. Fabry, O. Aumont, L. Bopp, S. C. Doney, R. A. Feely, A. Gnanadesikan, N. Gruber, A. Ishida, F. Joos, R. M. Key, K. Lindsay, E. Maier-Reimer, R. Matear, P. Monfray, A. Mouchet, R. G. Najjar, G.-K. Plattner, K. B. Rodgers, C. L. Sabine, J. L. Sarmiento, R. Schlitzer, R. D. Slater, I. J. Totterdell, M.-F. Weirig, Y. Yamanaka, A. Yool, Anthropogenic ocean acidification over the twenty-first century and its impact on calcifying organisms. *Nature* **437**, 681–686 (2005).
6. L. Kwiatkowski, O. Torres, L. Bopp, O. Aumont, M. Chamberlain, J. R. Christian, J. P. Dunne, M. Gehlen, T. Ilyina, J. G. John, A. Lenton, H. Li, N. S. Lovenduski, J. C. Orr, J. Palmieri, Y. Santana-Falcón, J. Schwinger, R. Séférian, C. A. Stock, A. Tagliabue, Y. Takano, J. Tjiputra, K. Toyama, H. Tsujino, M. Watanabe, A. Yamamoto, A. Yool, T. Ziehn, Twenty-first century ocean warming, acidification, deoxygenation, and upper-ocean nutrient and primary production decline from CMIP6 model projections. *Biogeosciences* **17**, 3439–3470 (2020).
7. K. J. Kroeker, R. L. Kordas, R. N. Crim, G. G. Singh, Meta-analysis reveals negative yet variable effects of ocean acidification on marine organisms. *Ecol. Lett.* **13**, 1419–1434 (2010).
8. S. C. Doney, D. S. Busch, S. R. Cooley, K. J. Kroeker, The Impacts of Ocean Acidification on Marine Ecosystems and Reliant Human Communities. *Annu. Rev. Environ. Resour.* **45**, 83–112 (2020).
9. V. J. Fabry, B. A. Seibel, R. A. Feely, J. C. Orr, Impacts of ocean acidification on marine fauna and ecosystem processes. *ICES J. Mar. Sci.* **65**, 414–432 (2008).
10. J. C. Orr, E. Maier-Reimer, U. Mikolajewicz, P. Monfray, J. L. Sarmiento, J. R. Toggweiler, N. K. Taylor, J. Palmer, N. Gruber, C. L. Sabine, C. Le Quéré, R. M. Key, J. Boutin, Estimates of anthropogenic carbon uptake from four three-dimensional global ocean models. *Glob. Biogeochem. Cycles* **15**, 43–60 (2001).
11. S. E. M. Fletcher, N. Gruber, A. R. Jacobson, S. C. Doney, S. Dutkiewicz, M. Gerber, M. Follows, F. Joos, K. Lindsay, D. Menemenlis, A. Mouchet, S. A. Müller, J. L. Sarmiento, Inverse estimates of anthropogenic CO2 uptake, transport, and storage by the ocean. *Glob. Biogeochem. Cycles* **20** (2006).
12. S. Khatiwala, F. Primeau, T. Hall, Reconstruction of the history of anthropogenic CO 2 concentrations in the ocean. *Nature* **462**, 346–349 (2009).
13. C. L. Sabine, R. A. Feely, N. Gruber, R. M. Key, K. Lee, J. L. Bullister, R. Wanninkhof, C. S. Wong, D. W. R. Wallace, B. Tilbrook, F. J. Millero, T.-H. Peng, A. Kozyr, T. Ono, A. F. Rios, The Oceanic Sink for Anthropogenic CO2. *Science* **305**, 367–371 (2004).
14. J. D. Müller, N. Gruber, B. Carter, R. Feely, M. Ishii, N. Lange, S. K. Lauvset, A. Murata, A. Olsen, F. F. Pérez, C. Sabine, T. Tanhua, R. Wanninkhof, D. Zhu, Decadal Trends in the Oceanic Storage of Anthropogenic Carbon From 1994 to 2014. *AGU Adv.* **4**, e2023AV000875 (2023).
15. X. Davila, G. Gebbie, A. Brakstad, S. K. Lauvset, E. L. McDonagh, J. Schwinger, A. Olsen, How Is the Ocean Anthropogenic Carbon Reservoir Filled? *Glob. Biogeochem. Cycles* **36**, e2021GB007055 (2022).
16. A. J. Fassbender, B. R. Carter, J. D. Sharp, Y. Huang, M. C. Arroyo, H. Frenzel, Amplified Subsurface Signals of Ocean Acidification. *Glob. Biogeochem. Cycles* **37**, e2023GB007843 (2023).
17. S. K. Lauvset, B. R. Carter, F. F. Pèrez, L.-Q. Jiang, R. A. Feely, A. Velo, A. Olsen, Processes Driving Global Interior Ocean pH Distribution. *Glob. Biogeochem. Cycles* **34**, e2019GB006229 (2020).
18. B. R. Carter, R. A. Feely, R. Wanninkhof, S. Kouketsu, R. E. Sonnerup, P. C. Pardo, C. L. Sabine, G. C. Johnson, B. M. Sloyan, A. Murata, S. Mecking, B. Tilbrook, K. Speer, L. D. Talley, F. J. Millero, S. E. Wijffels,

A. M. Macdonald, N. Gruber, J. L. Bullister, Pacific Anthropogenic Carbon Between 1991 and 2017. *Glob. Biogeochem. Cycles*, 2018GB006154 (2019).
19. N. Bednaršek, R. Feely, G. Pelletier, F. Desmet, Global Synthesis of the Status and Trends of Ocean Acidification Impacts on Shelled Pteropods. *Oceanography*, doi: 10.5670/oceanog.2023.210 (2023).
20. R. A. Feely, S. R. Alin, B. Carter, N. Bednaršek, B. Hales, F. Chan, T. M. Hill, B. Gaylord, E. Sanford, R. H. Byrne, C. L. Sabine, D. Greeley, L. Juranek, Chemical and biological impacts of ocean acidification along the west coast of North America. *Estuar. Coast. Shelf Sci.* **183**, 260–270 (2016).
21. A. Freiwald, J. H. Fossa, A. Grehan, T. K. and J. M. Roberts, "Cold Water Coral Reefs: Out of Sight-No Longer Out of Mind" (UNEP World Conservation Monitoring Centre (UNEP-WCMC), 2004); https://wedocs.unep.org/xmlui/handle/20.500.11822/8727.
22. J. M. Guinotte, J. Orr, S. Cairns, A. Freiwald, L. Morgan, R. George, Will human-induced changes in seawater chemistry alter the distribution of deep-sea scleractinian corals? *Front. Ecol. Environ.* **4**, 141–146 (2006).
23. S. J. Hennige, U. Wolfram, L. Wickes, F. Murray, J. M. Roberts, N. A. Kamenos, S. Schofield, A. Groetsch, E. M. Spiesz, M.-E. Aubin-Tam, P. J. Etnoyer, Crumbling Reefs and Cold-Water Coral Habitat Loss in a Future Ocean: Evidence of "Coralporosis" as an Indicator of Habitat Integrity. *Front. Mar. Sci.* **7**, 668 (2020).
24. B. A. Seibel, P. J. Walsh, Potential Impacts of CO2 Injection on Deep-Sea Biota. *Science* **294**, 319–320 (2001).
25. N. R. Bates, Multi-decadal uptake of carbon dioxide into subtropical mode water of the North Atlantic Ocean. *Biogeosciences* **9**, 2649–2659 (2012).
26. J. E. Dore, R. Lukas, D. W. Sadler, M. J. Church, D. M. Karl, Physical and biogeochemical modulation of ocean acidification in the central North Pacific. *Proc. Natl. Acad. Sci.* **106**, 12235–12240 (2009).
27. I. Skjelvan, S. K. Lauvset, T. Johannessen, K. Gundersen, Ø. Skagseth, Decadal trends in Ocean Acidification from the Ocean Weather Station M in the Norwegian Sea. *J. Mar. Syst.* **234**, 103775 (2022).
28. R. H. Byrne, S. Mecking, R. A. Feely, X. Liu, Direct observations of basin-wide acidification of the North Pacific Ocean. *Geophys. Res. Lett.* **37** (2010).
29. R. A. Feely, C. L. Sabine, R. H. Byrne, F. J. Millero, A. G. Dickson, R. Wanninkhof, A. Murata, L. A. Miller, D. Greeley, Decadal changes in the aragonite and calcite saturation state of the Pacific Ocean. *Glob. Biogeochem. Cycles* **26** (2012).
30. A. Murata, S. Saito, Decadal changes in the CaCO3 saturation state along 179°E in the Pacific Ocean. *Geophys. Res. Lett.* **39** (2012).
31. C. Li, Y. Wu, X. Wang, R. A. Feely, W.-J. Cai, L. Han, X. Lin, D. Qi, Accelerated Accumulation of Anthropogenic CO2 Drives Rapid Acidification in the North Pacific Subtropical Mode Water During 1993–2020. *Geophys. Res. Lett.* **49**, e2022GL101639 (2022).
32. A. Murata, K. Hayashi, Y. Kumamoto, K. Sasaki, Detecting the progression of ocean acidification from the saturation state of CaCO3 in the subtropical South Pacific. *Glob. Biogeochem. Cycles* **29**, 463–475 (2015).
33. M. Vázquez-Rodríguez, F. F. Pérez, A. Velo, A. F. Ríos, H. Mercier, Observed acidification trends in North Atlantic water masses. *Biogeosciences* **9**, 5217–5230 (2012).
34. E. F. Guallart, N. M. Fajar, X. A. Padín, M. Vázquez-Rodríguez, E. Calvo, A. F. Ríos, A. Hernández-Guerra, C. Pelejero, F. F. Pérez, Ocean acidification along the 24.5°N section in the subtropical North Atlantic. *Geophys. Res. Lett.* **42**, 450–458 (2015).
35. A. F. Ríos, L. Resplandy, M. I. García-Ibáñez, N. M. Fajar, A. Velo, X. A. Padin, R. Wanninkhof, R. Steinfeldt, G. Rosón, F. F. Pérez, Decadal acidification in the water masses of the Atlantic Ocean. *Proc. Natl. Acad. Sci.* **112**, 9950–9955 (2015).
36. R. E. Zeebe, D. A. Wolf-Gladrow, *CO2 in Seawater: Equilibrium, Kinetics, Isotopes* (Elsevier, 2001).
37. J. L. Sarmiento, N. Gruber, *Ocean Biogeochemical Dynamics* (Princeton University Press, 2006).
38. K. Caldeira, M. E. Wickett, Anthropogenic carbon and ocean pH. *Nature* **425**, 365–365 (2003).
39. R. A. Feely, C. L. Sabine, K. Lee, W. Berelson, J. Kleypas, V. J. Fabry, F. J. Millero, Impact of Anthropogenic CO2 on the CaCO3 System in the Oceans. *Science* **305**, 362–366 (2004).
40. L.-Q. Jiang, J. Dunne, B. R. Carter, J. F. Tjiputra, J. Terhaar, J. D. Sharp, A. Olsen, S. Alin, D. C. E. Bakker, R. A. Feely, J.-P. Gattuso, P. Hogan, T. Ilyina, N. Lange, S. K. Lauvset, E. R. Lewis, T. Lovato, J. Palmieri, Y. Santana-Falcón, J. Schwinger, R. Séférian, G. Strand, N. Swart, T. Tanhua, H. Tsujino, R. Wanninkhof, M. Watanabe, A. Yamamoto, T. Ziehn, Global Surface Ocean Acidification Indicators From 1750 to 2100. *J. Adv. Model. Earth Syst.* **15**, e2022MS003563 (2023).
41. A. Planchat, L. Kwiatkowski, L. Bopp, O. Torres, J. R. Christian, M. Butenschön, T. Lovato, R. Séférian, M. A. Chamberlain, O. Aumont, M. Watanabe, A. Yamamoto, A. Yool, T. Ilyina, H. Tsujino, K. M. Krumhardt, J. Schwinger, J. Tjiputra, J. P. Dunne, C. Stock, The representation of alkalinity and the carbonate pump from CMIP5 to CMIP6 Earth system models and implications for the carbon cycle. *Biogeosciences* **20**, 1195–1257 (2023).
42. C. Hinrichs, P. Köhler, C. Völker, J. Hauck, Alkalinity biases in CMIP6 Earth system models and implications for simulated CO_2 drawdown via artificial alkalinity enhancement. *Biogeosciences* **20**, 3717–3735 (2023).
43. K. Richardson, W. Steffen, W. Lucht, J. Bendtsen, S. E. Cornell, J. F. Donges, M. Drüke, I. Fetzer, G. Bala, W. von Bloh, G. Feulner, S. Fiedler, D. Gerten, T. Gleeson, M. Hofmann, W. Huiskamp, M. Kummu, C. Mohan,

D. Nogués-Bravo, S. Petri, M. Porkka, S. Rahmstorf, S. Schaphoff, K. Thonicke, A. Tobian, V. Virkki, L. Wang-Erlandsson, L. Weber, J. Rockström, Earth beyond six of nine planetary boundaries. *Sci. Adv.* **9**, eadh2458 (2023).
44. J. Rockström, W. Steffen, K. Noone, Å. Persson, F. S. Chapin, E. F. Lambin, T. M. Lenton, M. Scheffer, C. Folke, H. J. Schellnhuber, B. Nykvist, C. A. de Wit, T. Hughes, S. van der Leeuw, H. Rodhe, S. Sörlin, P. K. Snyder, R. Costanza, U. Svedin, M. Falkenmark, L. Karlberg, R. W. Corell, V. J. Fabry, J. Hansen, B. Walker, D. Liverman, K. Richardson, P. Crutzen, J. A. Foley, A safe operating space for humanity. *Nature* **461**, 472–475 (2009).
45. J. Rockström, W. Steffen, K. Noone, Å. Persson, F. S. I. Chapin, E. Lambin, T. Lenton, M. Scheffer, C. Folke, H. J. Schellnhuber, B. Nykvist, C. de Wit, T. Hughes, S. van der Leeuw, H. Rodhe, S. Sörlin, P. Snyder, R. Costanza, U. Svedin, M. Falkenmark, L. Karlberg, R. Corell, V. Fabry, J. Hansen, B. Walker, D. Liverman, K. Richardson, P. Crutzen, J. Foley, Planetary Boundaries: Exploring the Safe Operating Space for Humanity. *Ecol. Soc.* **14** (2009).
46. N. Gruber, J. L. Sarmiento, T. F. Stocker, An improved method for detecting anthropogenic CO2 in the oceans. *Glob. Biogeochem. Cycles* **10**, 809–837 (1996).
47. D. Clement, N. Gruber, The eMLR(C*) Method to Determine Decadal Changes in the Global Ocean Storage of Anthropogenic CO_2. *Glob. Biogeochem. Cycles* **32**, 654–679 (2018).
48. S. K. Lauvset, R. M. Key, A. Olsen, S. van Heuven, A. Velo, X. Lin, C. Schirnick, A. Kozyr, T. Tanhua, M. Hoppema, S. Jutterström, R. Steinfeldt, E. Jeansson, M. Ishii, F. F. Perez, T. Suzuki, S. Watelet, A new global interior ocean mapped climatology: the 1◦ × 1◦ GLODAP version 2. 16 (2016).
49. R. Locarnini, A. Mishonov, O. Baranova, T. Boyer, M. Zweng, H. Garcia, J. Reagan, D. Seidov, K. Weathers, C. Paver, I. Smolyar, R. Locarnini, "World Ocean Atlas 2018, Volume 1: Temperature" (2019).
50. M. M. Zweng, J. Reagan, D. Seidov, T. Boyer, R. Locarnini, H. Garcia, A. Mishonov, O. K. Baranova, C. Paver, I. Smolyar, "WORLD OCEAN ATLAS 2018 Volume 2: Salinity" (2019).
51. D. Ma, L. Gregor, N. Gruber, Four Decades of Trends and Drivers of Global Surface Ocean Acidification. *Glob. Biogeochem. Cycles* **37**, e2023GB007765 (2023).
52. T. DeVries, The oceanic anthropogenic CO2 sink: Storage, air-sea fluxes, and transports over the industrial era. *Glob. Biogeochem. Cycles* **28**, 631–647 (2014).
53. X. Lan, P. Tans, K. W. Thoning, Trends in globally-averaged CO2 determined from NOAA Global Monitoring Laboratory measurements. Version 2022-11 NOAA/GML (gml.noaa.gov/ccgg/trends/) (2022).
54. N. Gruber, Consistent patterns of nitrogen fixation identified in the ocean. *Nature* **566**, 191–193 (2019).
55. M. Steinacher, F. Joos, T. L. Frölicher, G.-K. Plattner, S. C. Doney, Imminent ocean acidification in the Arctic projected with the NCAR global coupled carbon cycle-climate model. *Biogeosciences* **6**, 515–533 (2009).
56. G. Negrete-García, N. S. Lovenduski, C. Hauri, K. M. Krumhardt, S. K. Lauvset, Sudden emergence of a shallow aragonite saturation horizon in the Southern Ocean. *Nat. Clim. Change* **9**, 313–317 (2019).
57. C. Hauri, S. C. Doney, T. Takahashi, M. Erickson, G. Jiang, H. W. Ducklow, Two decades of inorganic carbon dynamics along the West Antarctic Peninsula. *Biogeosciences* **12**, 6761–6779 (2015).
58. A. Freiwald, A. Rogers, J. Hall-Spencer, J. M. Guinotte, A. J. Davies, C. Yesson, C. Martin, L. V. Weatherdon, Global distribution of cold-water corals (version 5.1). Fifth update to the dataset in Freiwald et al. (2004) by UNEP-WCMC, in collaboration with Andre Freiwald and John Guinotte. Cambridge (UK, version 5.1, United Nations Environment Programme World Conservation Monitoring Centre (UNEP-WCMC) (2021); https://doi.org/10.34892/72X9-RT61.
59. M.-D. Zheng, L. Cao, Simulation of global ocean acidification and chemical habitats of shallow- and cold-water coral reefs. *Adv. Clim. Change Res.* **5**, 189–196 (2014).
60. F. Joos, T. L. Frölicher, M. Steinacher, G.-K. Plattner, "Impact of Climate Change Mitigation on Ocean Acidification Projections" in *Ocean Acidification*, J.-P. Gattuso, L. Hansson, Eds. (Oxford University Press, 2011; https://doi.org/10.1093/oso/9780199591091.003.0019), p. 0.
61. E. T. Buitenhuis, C. Le Quéré, N. Bednaršek, R. Schiebel, Large Contribution of Pteropods to Shallow CaCO3 Export. *Glob. Biogeochem. Cycles* **33**, 458–468 (2019).
62. N. Bednaršek, J. Možina, M. Vogt, C. O'Brien, G. A. Tarling, The global distribution of pteropods and their contribution to carbonate and carbon biomass in the modern ocean. *Earth Syst. Sci. Data* **4**, 167–186 (2012).
63. L. Keppler, P. Landschützer, S. K. Lauvset, N. Gruber, Recent Trends and Variability in the Oceanic Storage of Dissolved Inorganic Carbon. *Glob. Biogeochem. Cycles* **37**, e2022GB007677 (2023).
64. L. Cheng, G. Foster, Z. Hausfather, K. E. Trenberth, J. Abraham, Improved Quantification of the Rate of Ocean Warming. *J. Clim.* **35**, 4827–4840 (2022).
65. J.-P. Gattuso, J.-M. Epitalon, H. Lavigne, J. Orr, seacarb: Seawater Carbonate Chemistry, (2021); https://CRAN.R-project.org/package=seacarb.
66. O. Sulpis, S. K. Lauvset, M. Hagens, Current estimates of K1* and K2* appear inconsistent with measured CO2 system parameters in cold oceanic regions. *Ocean Sci.* **16**, 847–862 (2020).
67. A. G. Dickson, J. P. Riley, The estimation of acid dissociation constants in seawater media from potentionmetric titrations with strong base. I. The ionic product of water — Kw. *Mar. Chem.* **7**, 89–99 (1979).

68. A. G. Dickson, Standard potential of the reaction: AgCl(s) + 12H2(g) = Ag(s) + HCl(aq), and and the standard acidity constant of the ion HSO4− in synthetic sea water from 273.15 to 318.15 K. *J. Chem. Thermodyn.* **22**, 113–127 (1990).
69. E. S. Egleston, C. L. Sabine, F. M. M. Morel, Revelle revisited: Buffer factors that quantify the response of ocean chemistry to changes in DIC and alkalinity: REVELLE REVISITED. *Glob. Biogeochem. Cycles* **24**, n/a-n/a (2010).
70. A. R. Longhurst, "Chapter 7 - PROVINCES: THE SECONDARY COMPARTMENTS" in *Ecological Geography of the Sea (Second Edition)*, A. R. Longhurst, Ed. (Academic Press, Burlington, 2007; https://www.sciencedirect.com/science/article/pii/B9780124555211500085), pp. 103–114.

Acknowledgments

The authors thank all colleagues that supported and contributed to the collection and harmonization of the high-quality ocean interior observations made available through GLODAP.

Funding

JDM and NG acknowledge support from the European Union's Horizon 2020 research and innovation programme under grant agreements no. 821003 (project 4C) and no. 821001 (SO-CHIC).

Author contributions

Conceptualization: JDM, NG
Methodology: JDM, NG
Investigation: JDM
Visualization: JDM
Supervision: JDM, NG
Writing—original draft: JDM
Writing—review & editing: JDM, NG

Competing interests

Authors declare that they have no competing interests.

Data and materials availability

All data are available in the main text or the supplementary materials.

The anthropogenic carbon estimates used in this study are available through NCEI's Ocean Carbon and Acidification Data System (OCADS) via the digital object identifier:
https://doi.org/10.25921/ppcf-w020

The merged master file of GLODAPv2.2021 as well as the mapped climatology based on GLODAPv2 were accessed through:
www.glodap.info

The World Ocean Atlas 2018 climatology data and basin masks were accessed through:
https://www.ncei.noaa.gov/products/world-ocean-atlas

The code underlying this study is available through Github, and will be archived at Zenodo upon acceptance for publication:
https://github.com/jens-daniel-mueller/ocean_interior_acidification

The ocean interior acidification estimates as an outcome of this study will be made available through NCEI's Ocean Carbon and Acidification Data System (OCADS) upon acceptance of the manuscript for publication. The digital object identifier will be provided here. For review purposes, the outcome can be accessed through the ETH Zurich Research Collection under doi: 10.3929/ethz-b-000655933

Science Advances
AAAS

Supplementary Materials for

Progression of Ocean Interior Acidification over the Industrial Era

Jens D. Müller, Nicolas Gruber

*Corresponding author. Email: jensdaniel.mueller@usys.ethz.ch

This PDF file includes:

Figs. S1 to S17

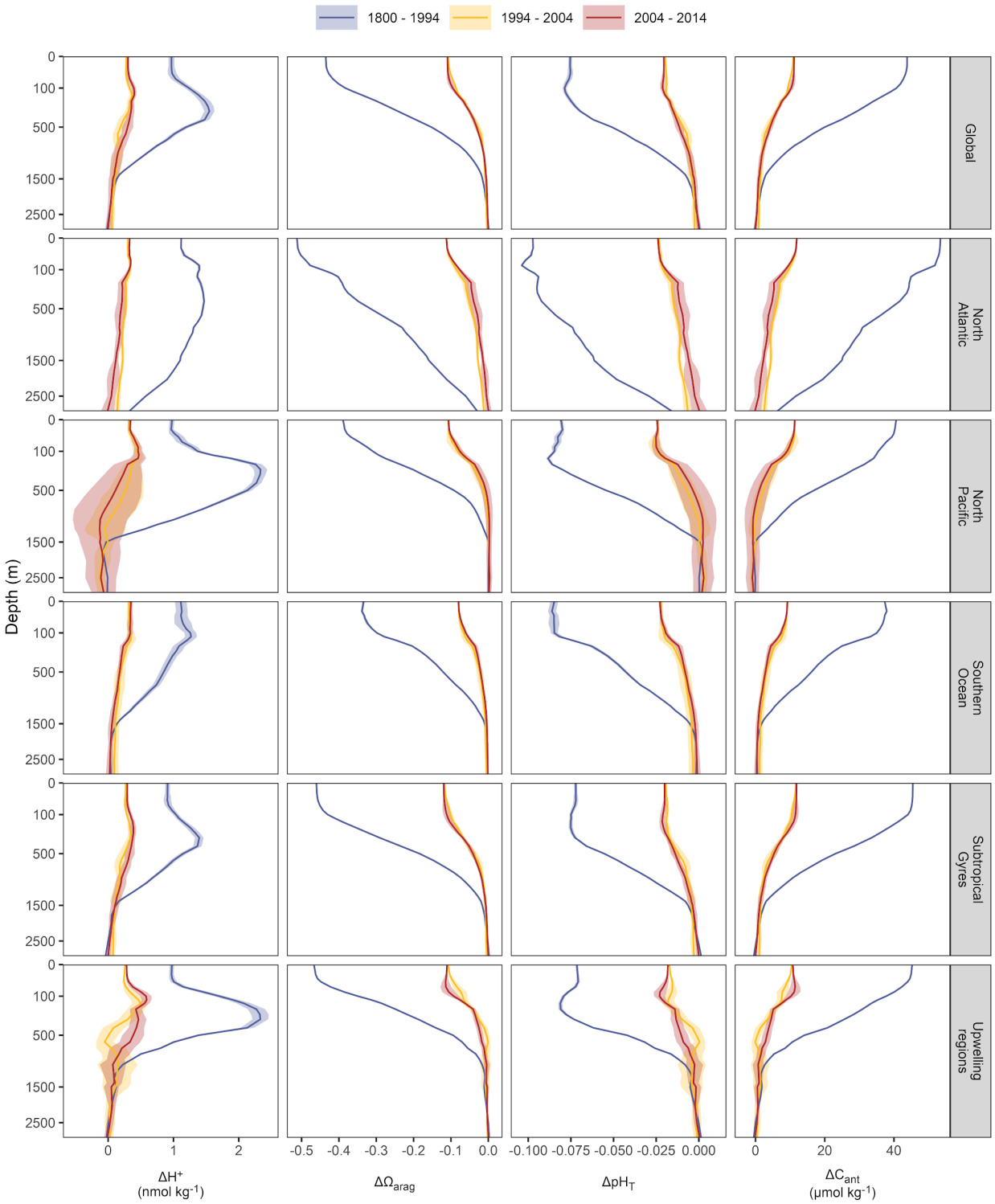

Fig. S1.

Same as Fig. 1, but showing incremental changes between reference years instead of total changes since 1800. CO_2 system sensitivities are not displayed.

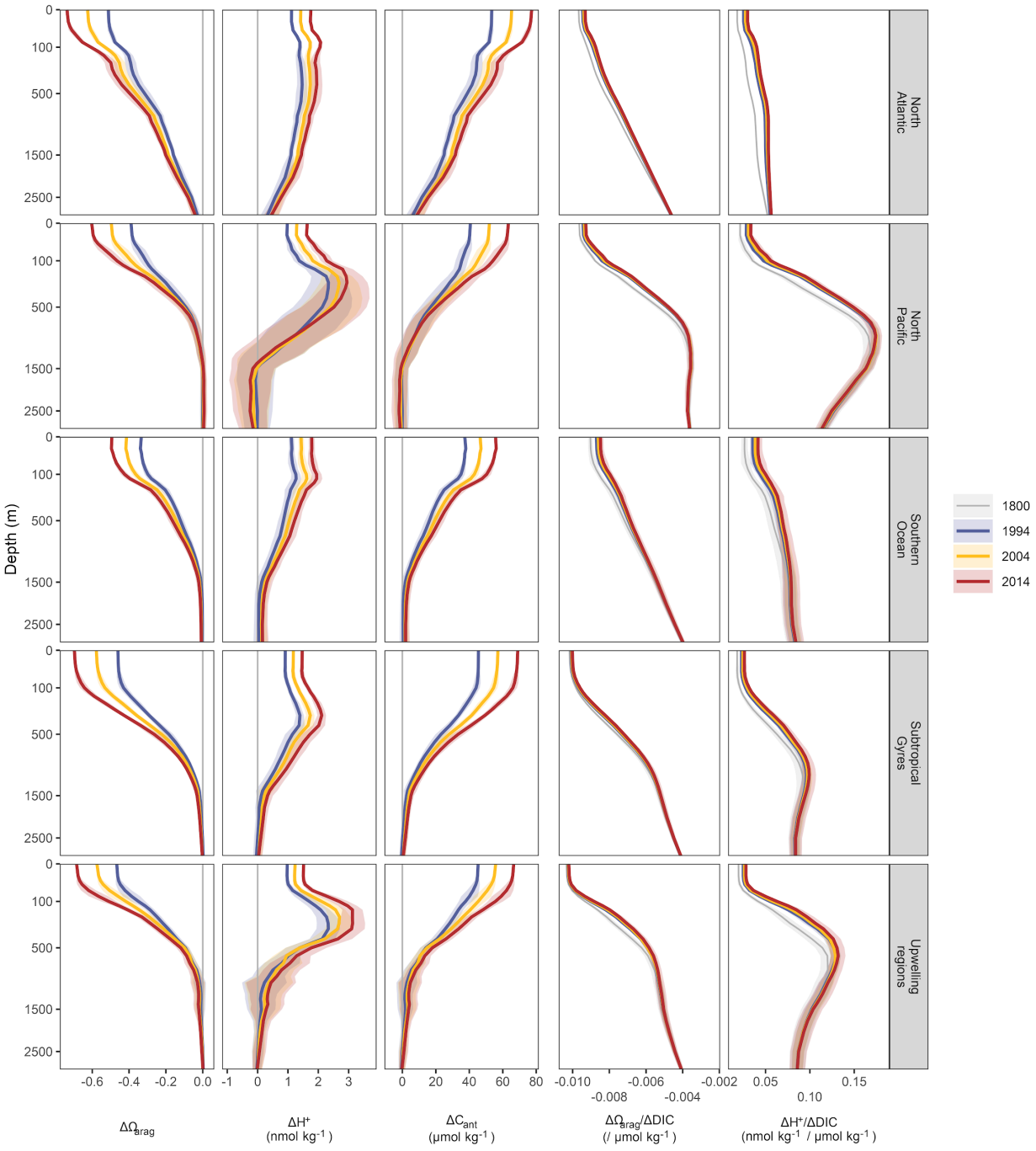

Fig. S2.

Same as Fig. 1, but averaged across individual ocean biomes according to Fig. S17.

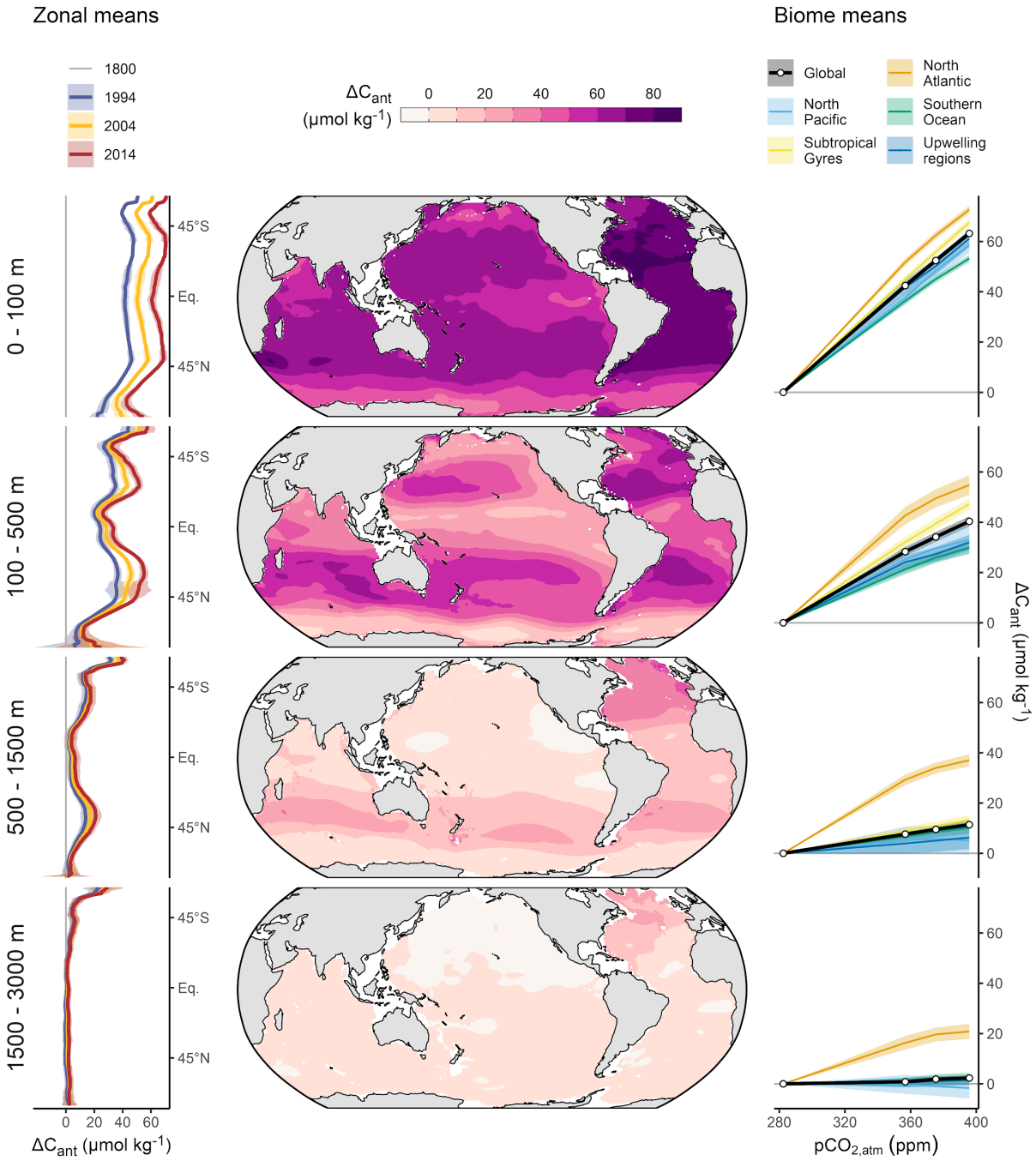

Fig. S3.

Same as Fig. 2, but for changes in the anthropogenic carbon content (ΔC_{ant}).

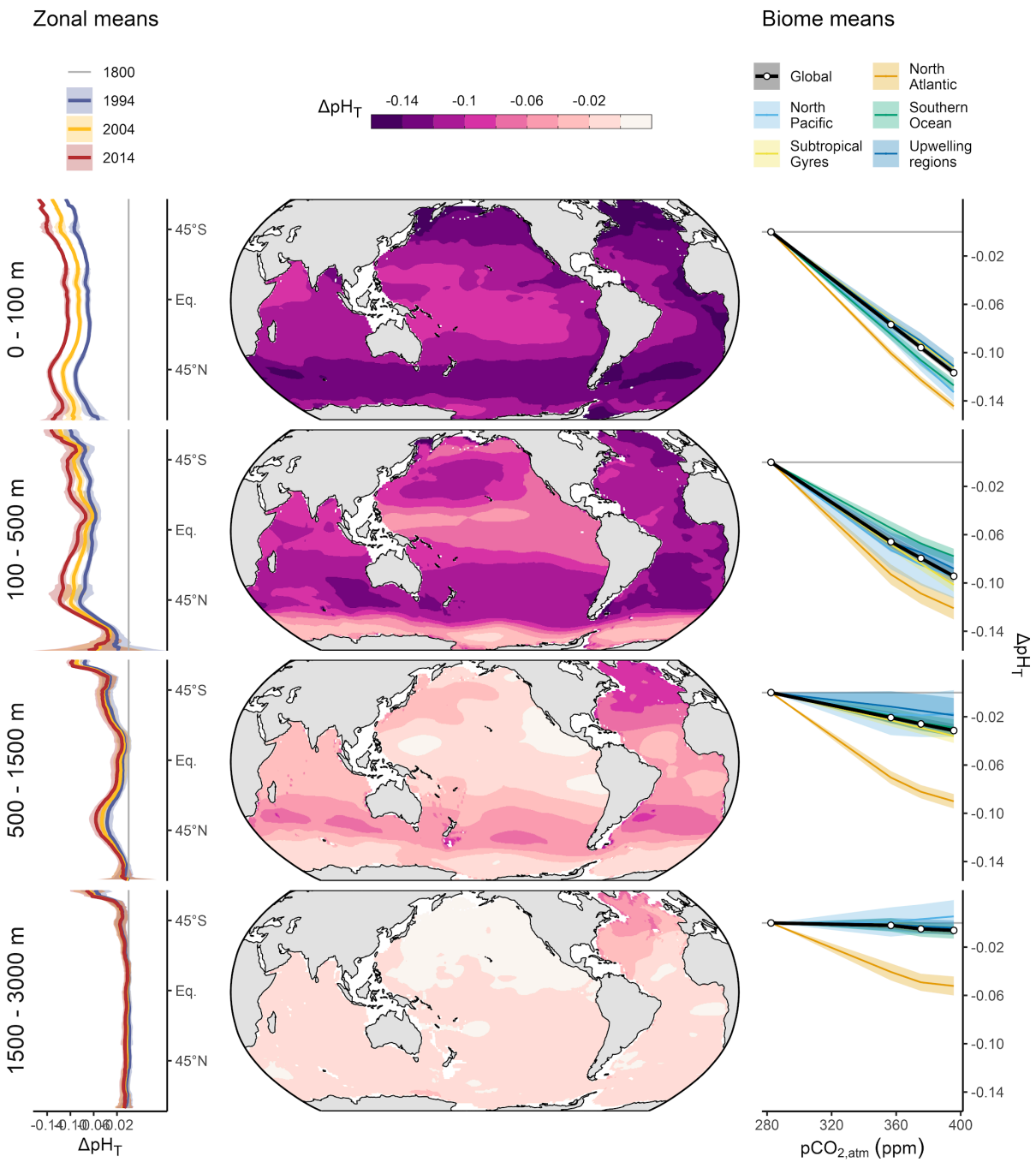

Fig. S4.

Same as Fig. 2, but for changes in pH on the total scale (ΔpH_T).

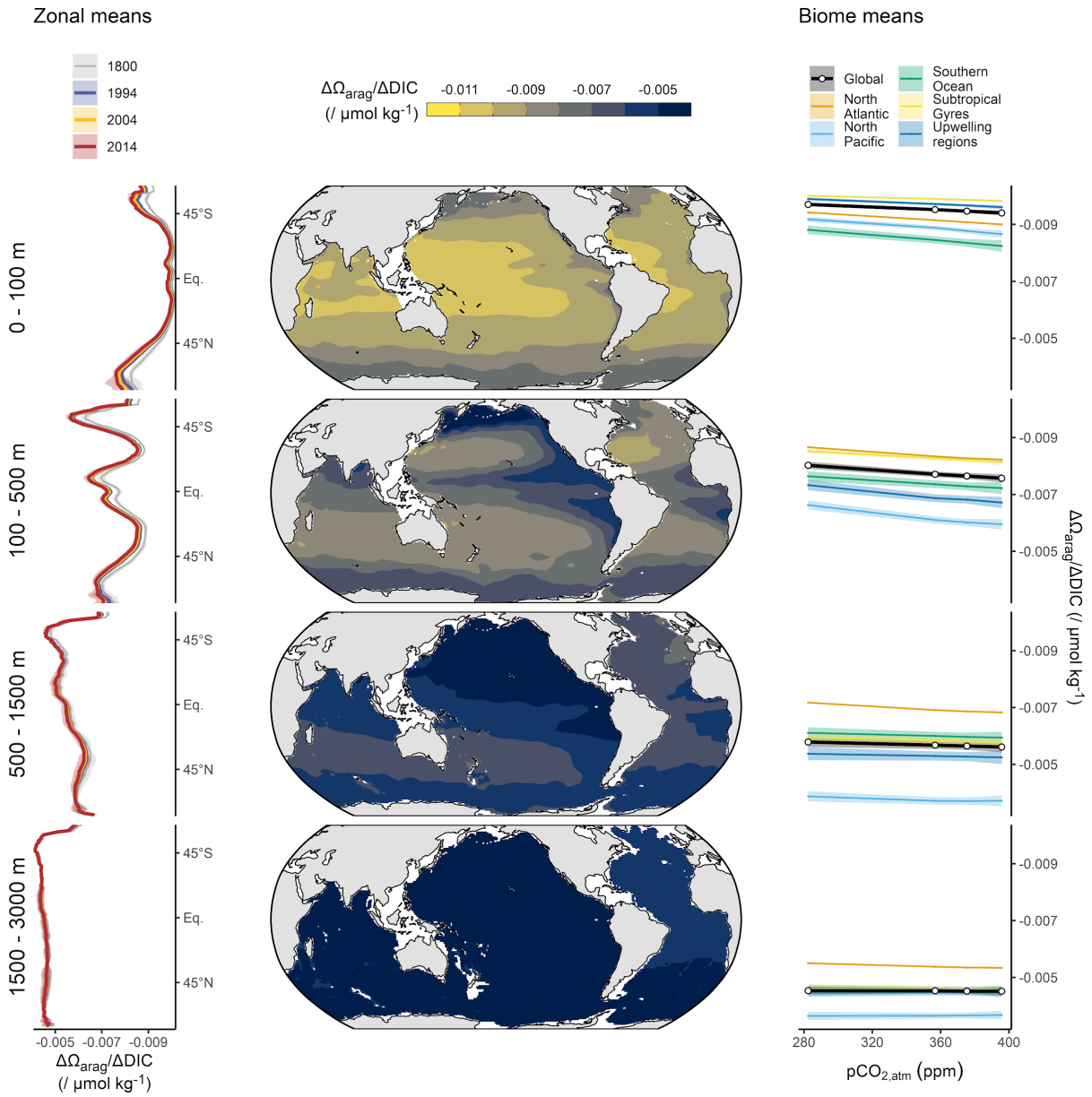

Fig. S5.

Sensitivity of the saturation state of aragonite to a change in the dissolved inorganic carbon concentration ($\Delta\Omega_{arag}/\Delta DIC$) averaged over four depth layers (rows). Central panels show maps of $\Delta\Omega_{arag}/\Delta DIC$ in 2014. Left panels show zonal mean $\Delta\Omega_{arag}/\Delta DIC$ for the reference years 1800, 1994, 2004 and 2014. Right panels show the global and regional mean $\Delta\Omega_{arag}/\Delta DIC$ as a function of the increase in atmospheric CO_2.

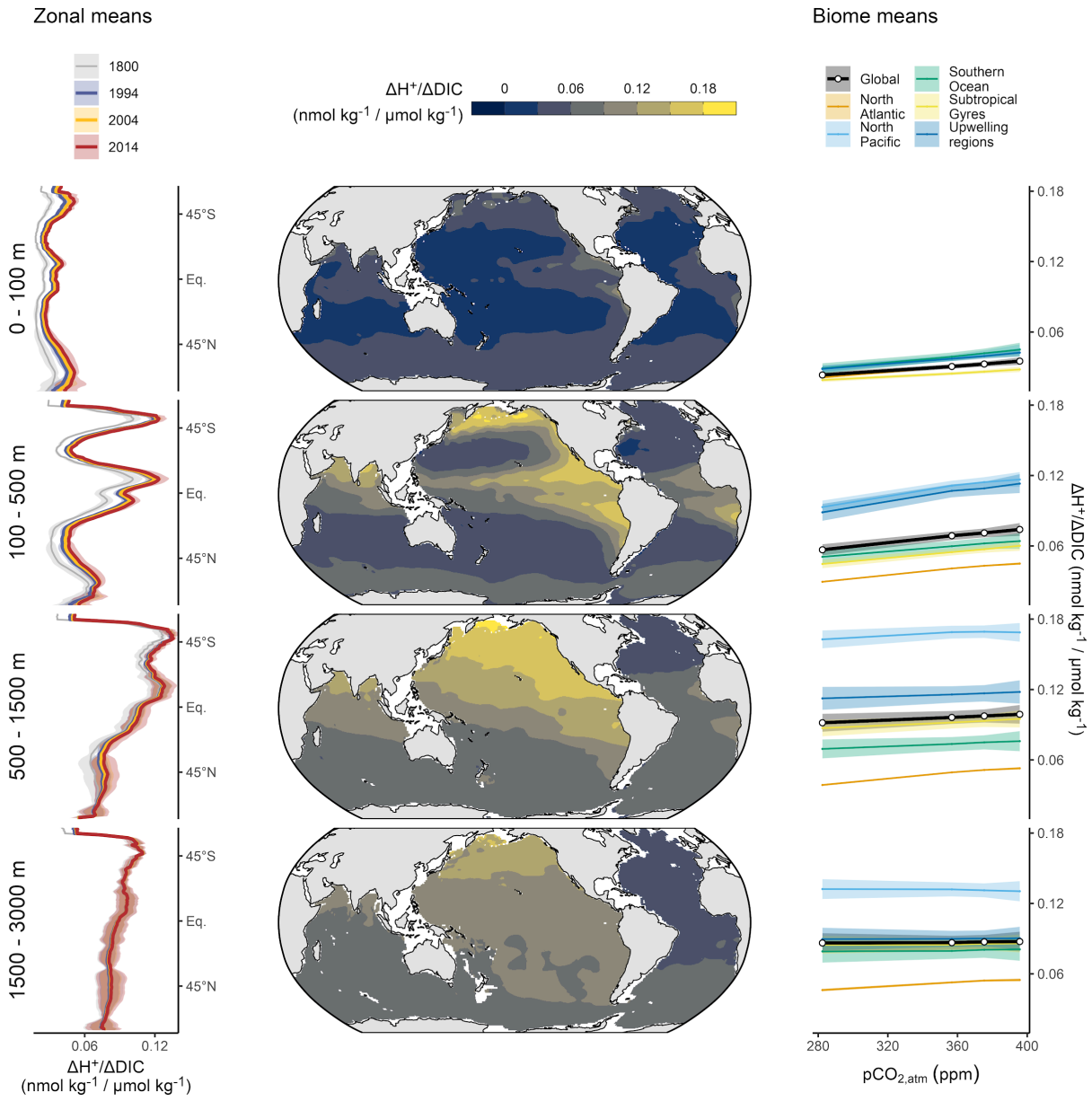

Fig. S6.

Same as Fig. S5, but for the sensitivity of the free proton concentration to a change in the dissolved inorganic carbon concentration ($\Delta H^+/\Delta DIC$).

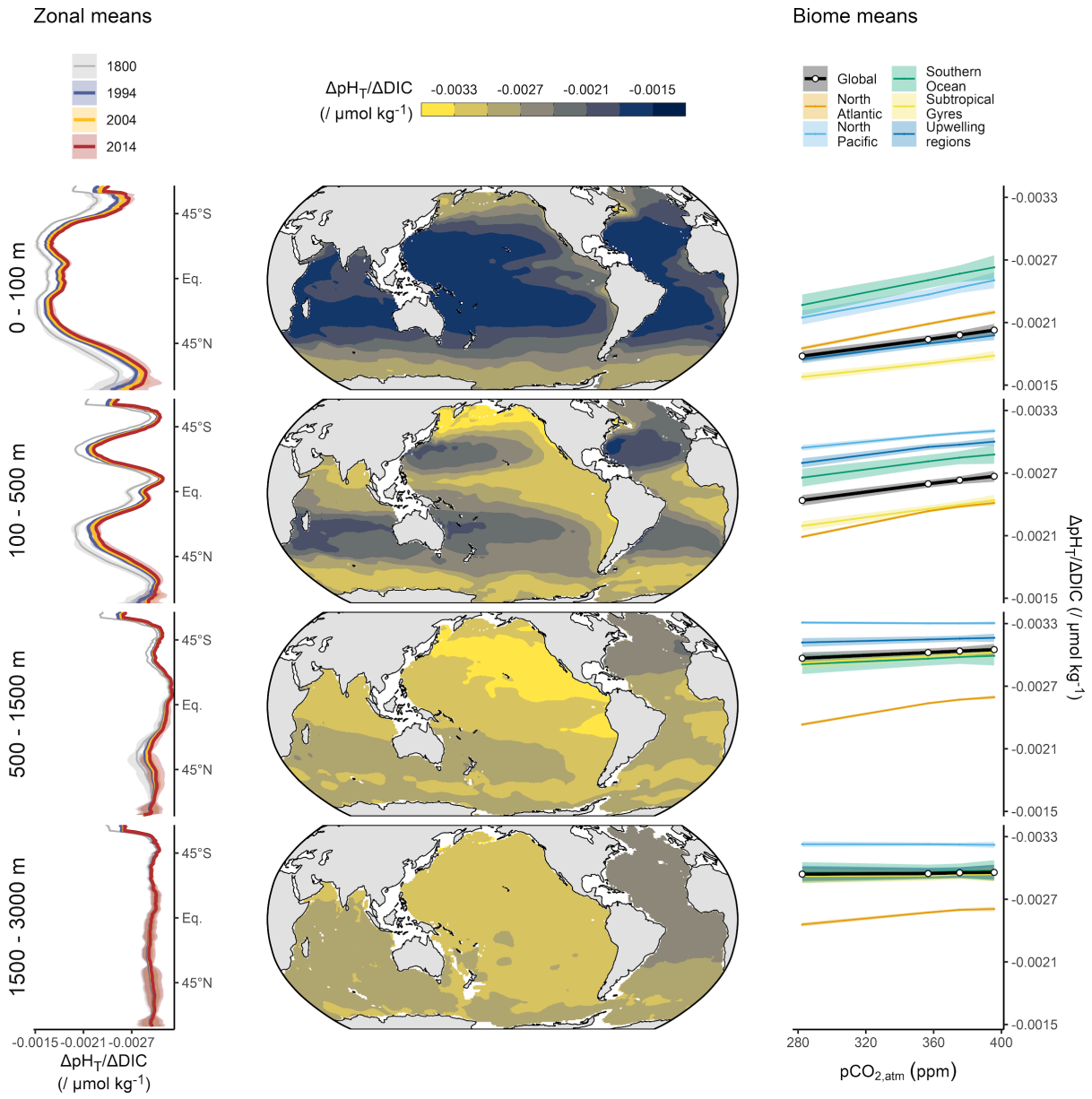

Fig. S7.

Same as Fig. S5, but for the sensitivity of pH on the total scale to a change in the dissolved inorganic carbon concentration ($\Delta pH_T/\Delta DIC$).

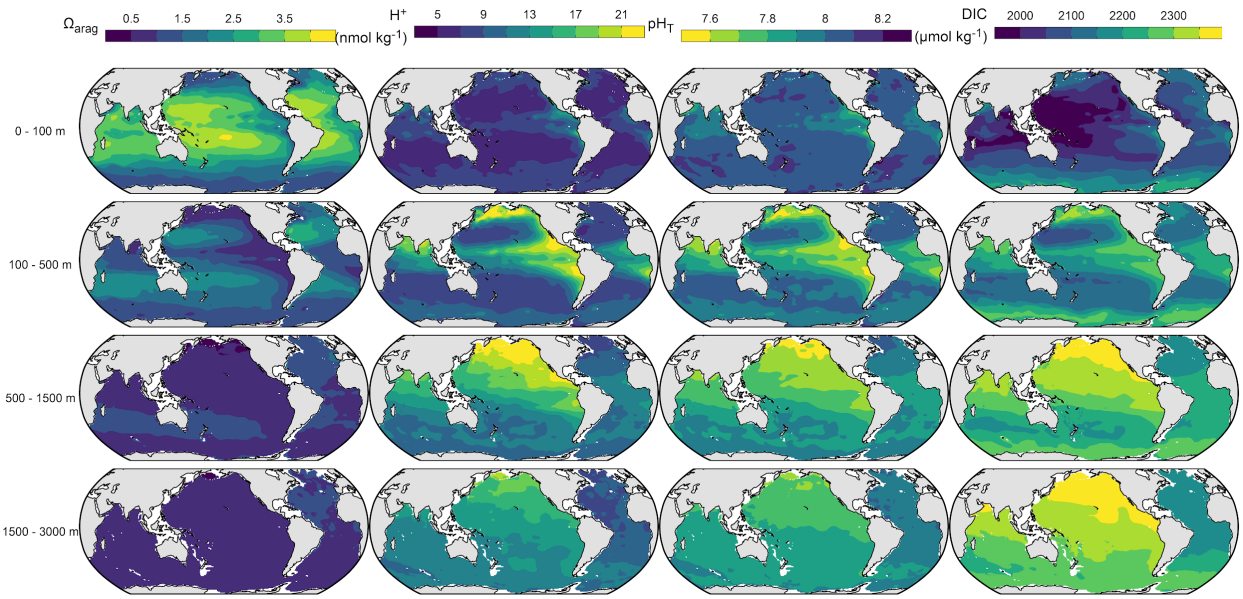

Fig. S8.

Absolute levels of the saturation state of aragonite (Ω_{arag}), the free proton concentration (H^+), pH on the total scale (pH_T) and dissolved inorganic carbon concentration (DIC) in 2014 averaged over four depth layers (rows).

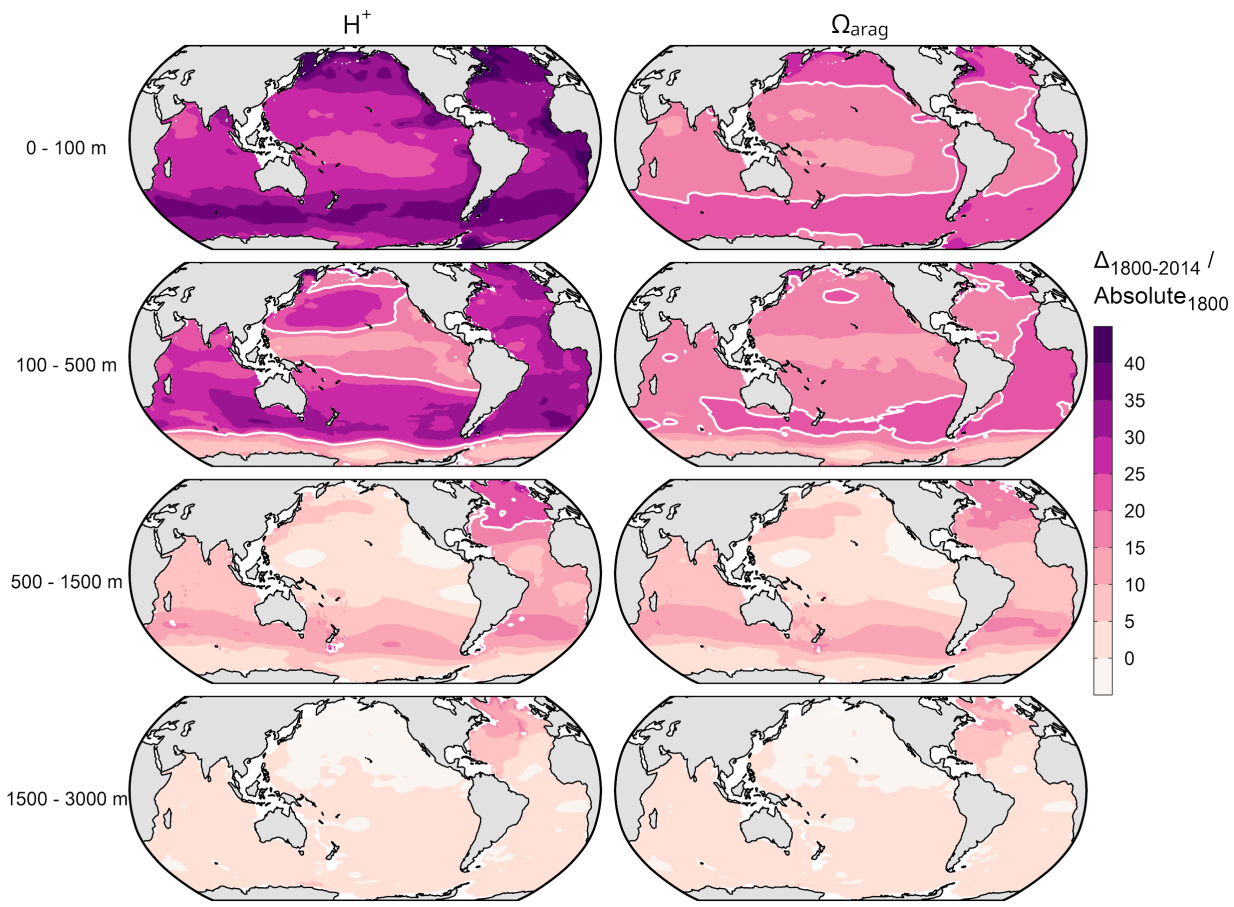

Fig. S9.

Acidification trends over the industrial era (1800-2014) in absolute terms and relative to the preindustrial value of the free proton content (ΔH^+, left panels) and the saturation state of aragonite ($\Delta\Omega_{arag}$, right panels) averaged over four depth layers (rows). White contour lines highlight relative changes of 30%.

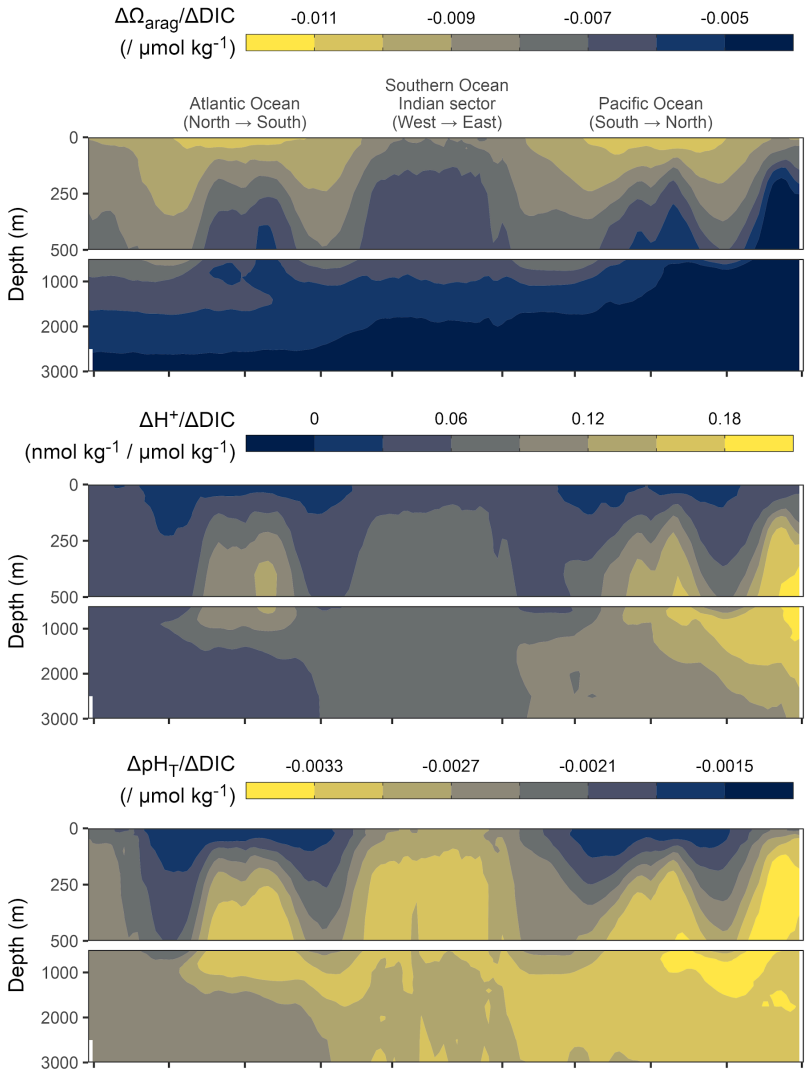

Fig. S10.

Global mean sections of the sensitivity of the saturation state of aragonite ($\Delta\Omega_{arag}$), the free proton content (ΔH^+), and pH on the total scale (pH_T) to a change in the dissolved inorganic carbon content (ΔDIC).

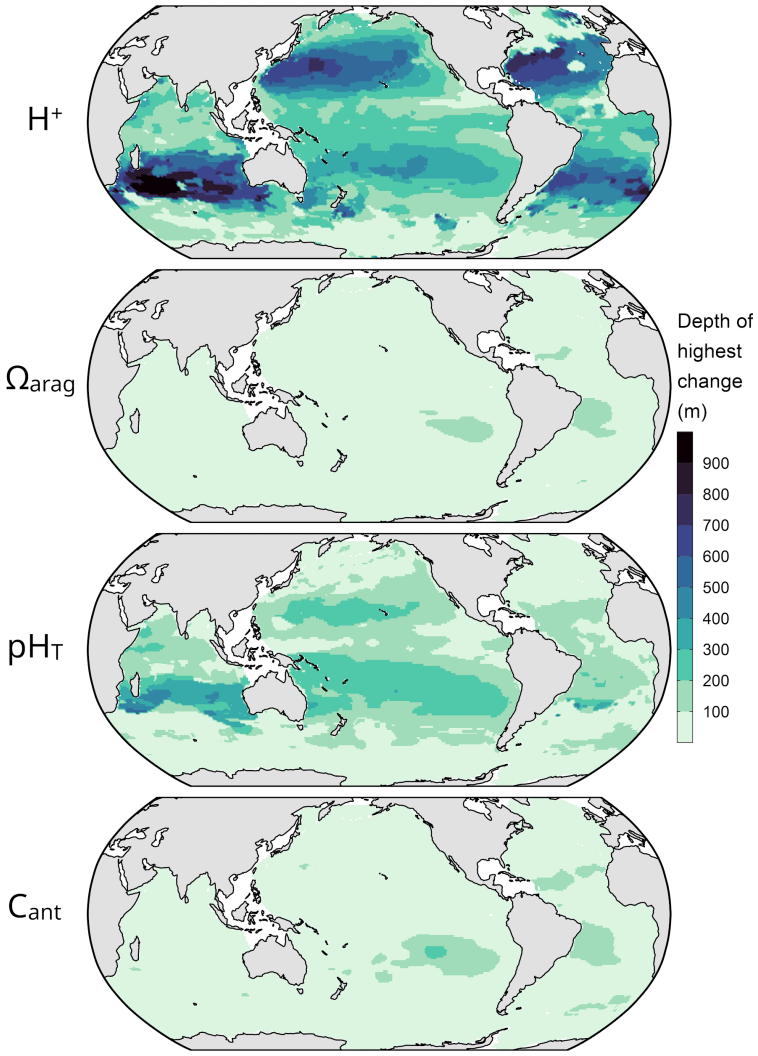

Fig. S11.

Depth of the highest absolute changes in the free proton concentration (H^+), the saturation state of aragonite (Ω_{arag}), pH on the total scale (pH_T) and anthropogenic carbon concentration (C_{ant}) from 1800 through 2014.

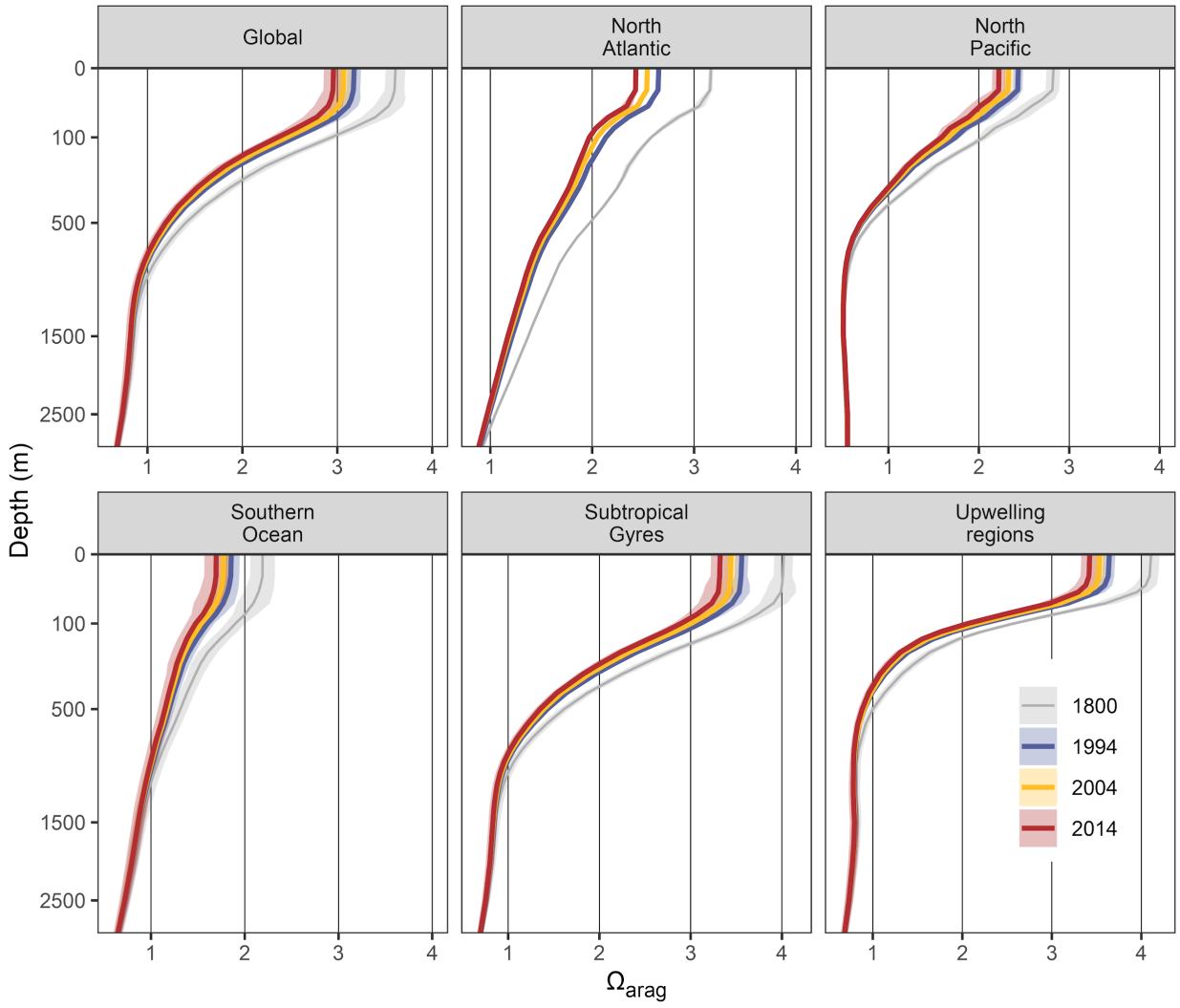

Fig. S12.

Mean vertical profiles of the saturation state of aragonite (Ω_{arag}) averaged over five ocean regions (Fig. S17) and globally, showing absolute values for four reference years between 1800 and 2014.

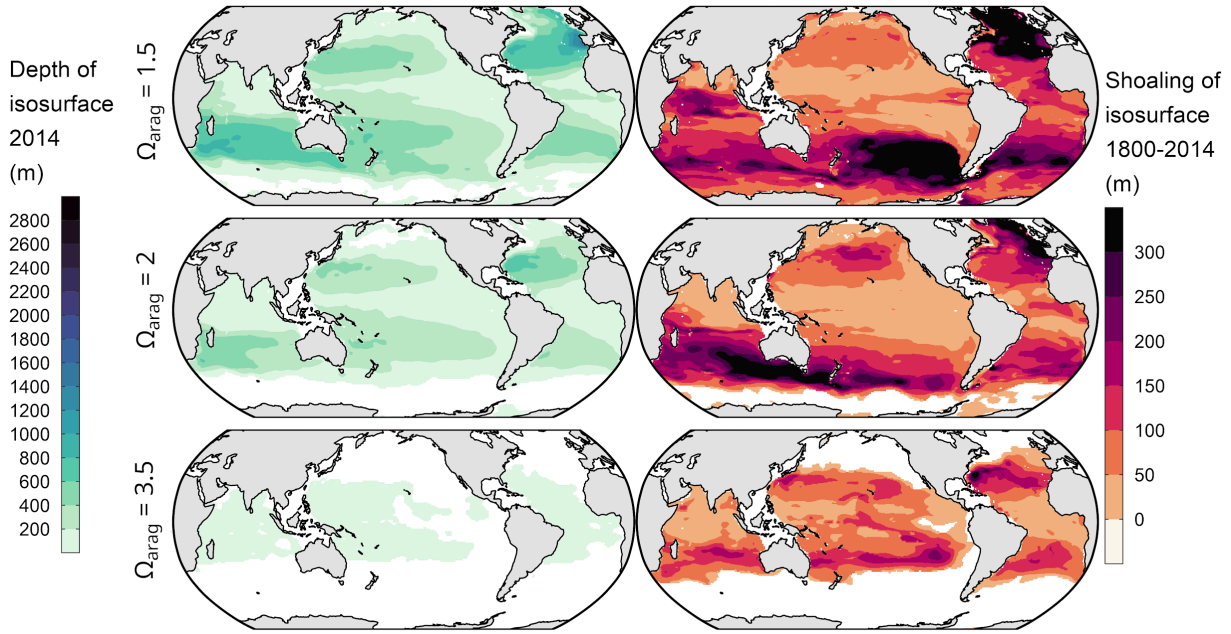

Fig. S13.

Same as Fig.68, but for the saturation thresholds 1.5, 2, and 3.5.

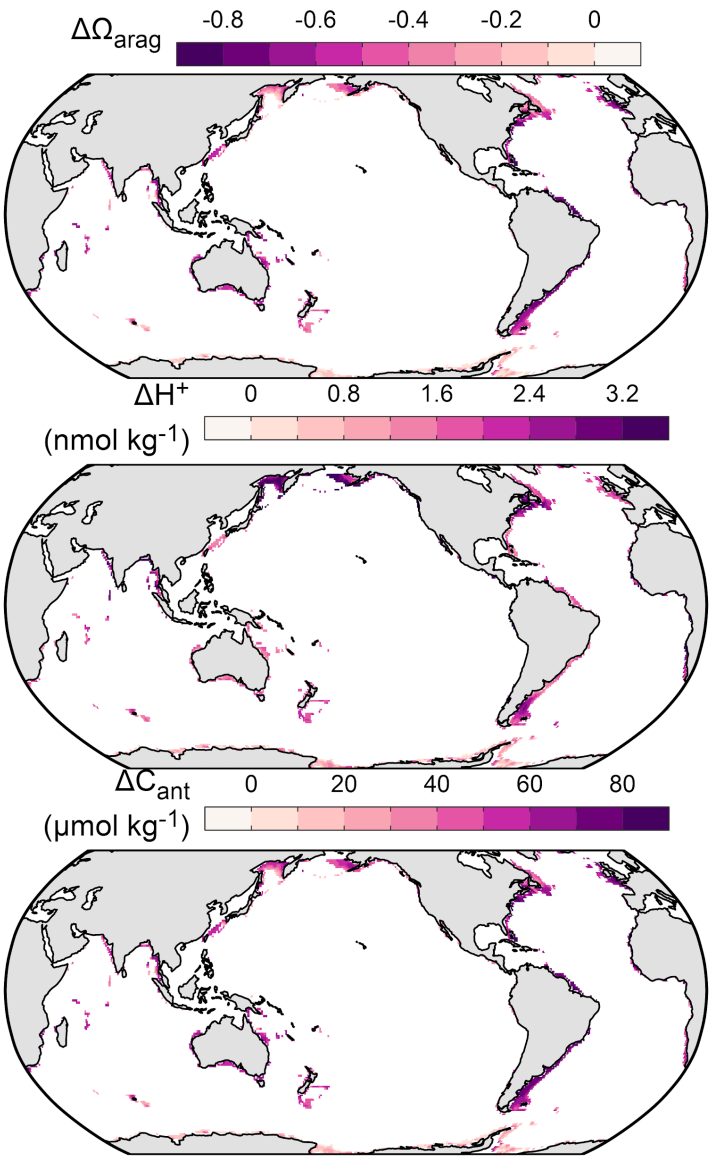

Fig. S14.

Acidification at the seafloor located within the top 500 m of the ocean, displayed for changes in the saturation state of aragonite ($\Delta\Omega_{arag}$), free proton concentration (ΔH^{+}), and anthropogenic carbon concentration (ΔC_{ant}).

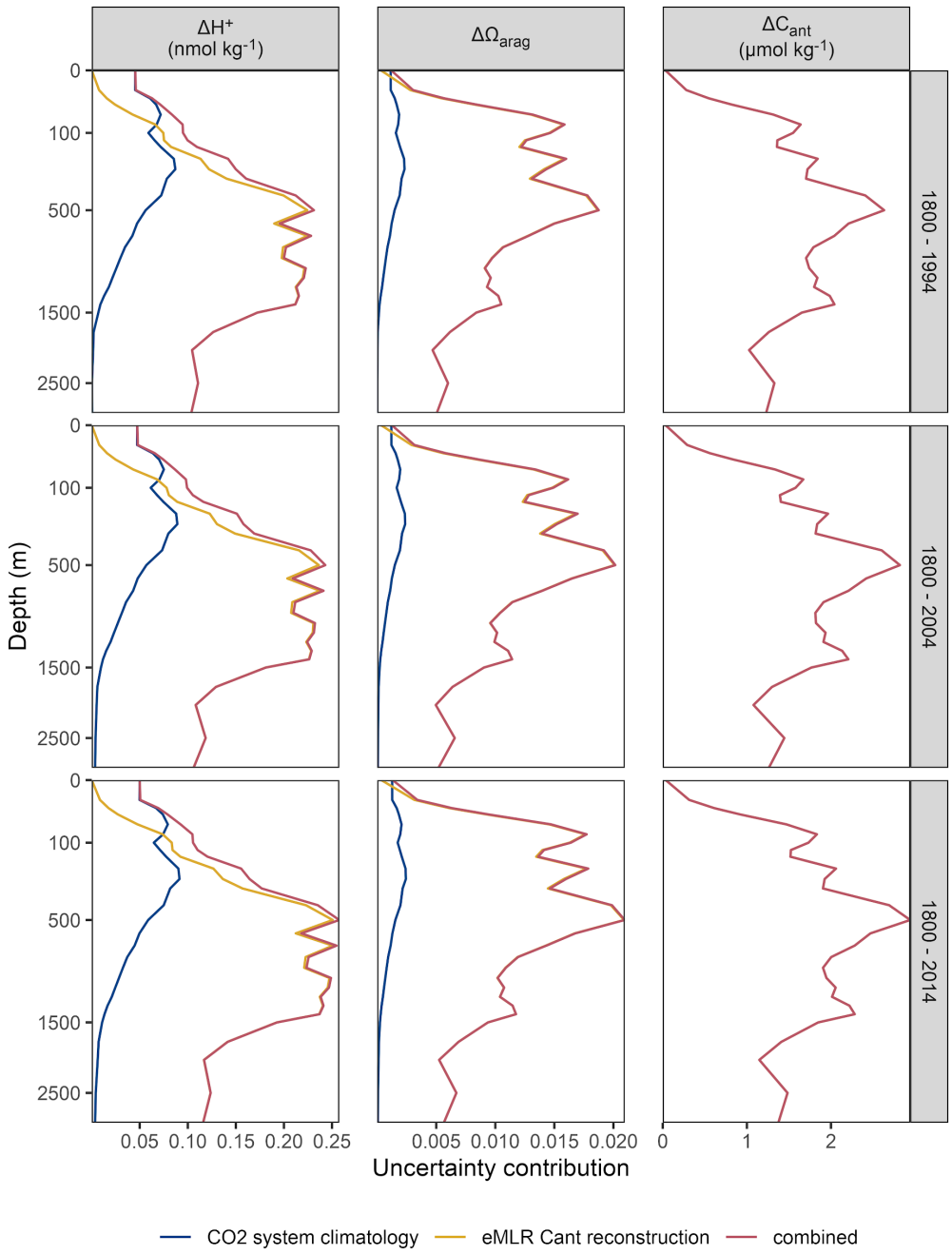

Fig. S15.

Global mean vertical profiles of the contributions to the uncertainty in changes in the saturation state of aragonite ($\Delta\Omega_{arag}$), free proton concentrations (ΔH^+), and anthropogenic carbon concentration (ΔC_{ant}). Panel columns distinguish changes since 1800 for the reference years 1994, 2004, and 2014.

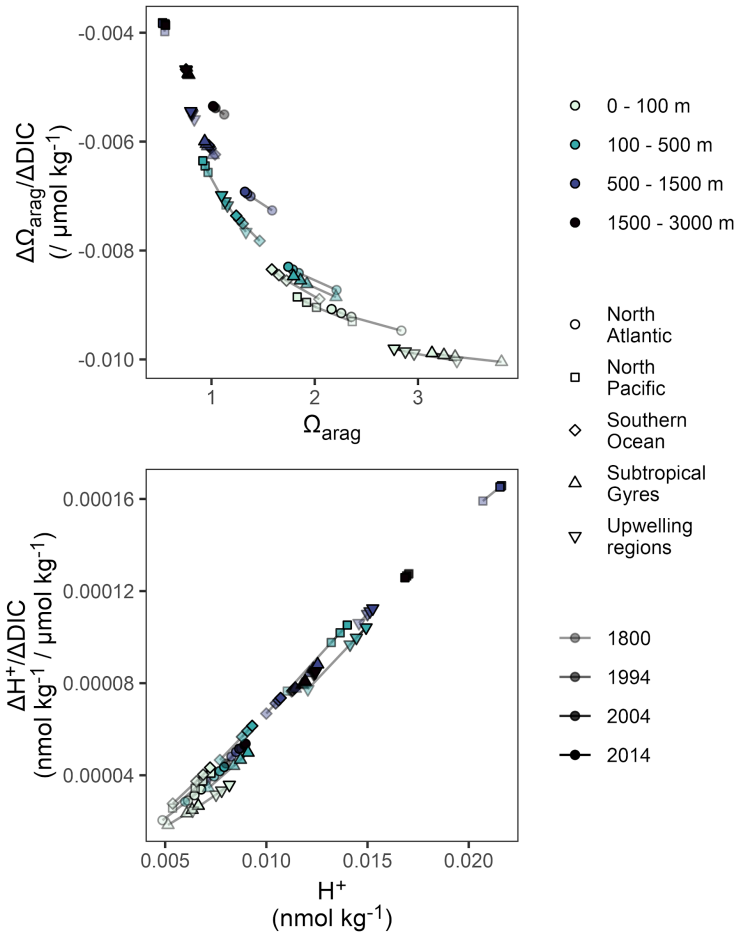

Fig. S16.

Sensitivity of the free proton concentration (H^+) and the saturation state of aragonite (Ω_{arag}) to a change in DIC as a function of their absolute value. The relationship is displayed for the mean state of the CO_2 system across the 5 regions (symbol shape), four depth layers (color) and four reference years (transparency) analyzed in this study. Estimates of the same region and depth layer are connected by a line to emphasize the temporal evolution.

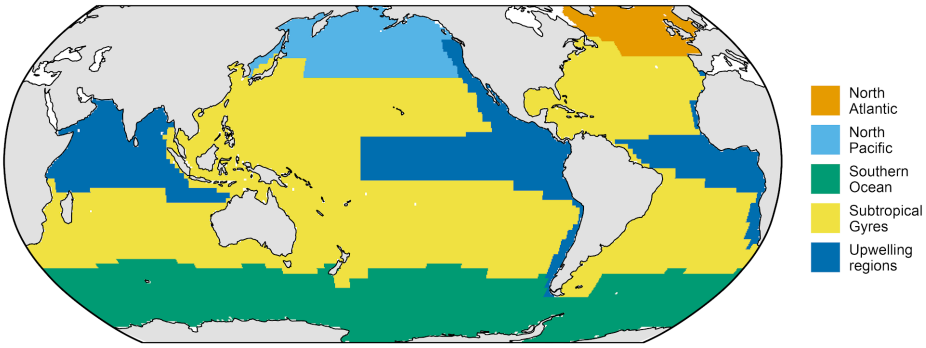

Fig. S17.

Ocean regions used to average ocean acidification trends in the horizontal dimension, based on aggregated provinces from Longhurst (2007).